# Hybrid Frequency-domain Modeling and Stability Analysis for Power Systems with Grid-following and Grid-forming Converters

Ni Liu, Hong Wang, Weihua Zhou, Jie Song, Yiting Zhang, Eduardo Prieto-Araujo, and Zhe Chen, *IEEE*, *Member*

***Abstract*—With the increase of the renewable energy generator capacity, the requirements of the power system for grid-connected converters are evolve, which leads to diverse control schemes and increased complexity of systematic stability analysis. Although various frequency-domain models are developed to identify oscillation causes, the discrepancies between them are rarely studied. This study aims to clarify these discrepancies and provide circuit insights for stability analysis by using different frequency-domain models. This study emphasizes the limitations of assuming that the transfer function of the self-stable converter does not have right half-plane (RHP) poles. To ensure that the self-stable converters are represented by a frequency-domain model without RHP poles, the applicability of this model of grid-following (GFL) and grid-forming (GFM) converters is discussed. This study recommends that the GFM converters with ideal sources should be represented in parallel with the $P/Q$-$\theta/V$ admittance model rather than the $V$-$I$ impedance model. Two cases are conducted to illustrate the rationality of the $P/Q$-$\theta/V$ admittance model. Additionally, a hybrid frequency-domain modeling framework and stability criteria are proposed for the power system with several GFL and GFM converters. The stability criteria eliminates the need to check the RHP pole numbers in the non-passive subsystem when applying the Nyquist stability criterion, thereby reducing the complexity of stability analysis. Simulations are carried out to validate the correctness of the frequency-domain model and the stability criteria.**

***Index Terms*—Converter, grid-forming (GFM), grid-following (GFL) impedance, renewable energy, stability analysis, frequency-domain model.**

Manuscript received: November 2, 2023; revised: March 8, 2024; accepted: September 3, 2024. Date of CrossCheck: September 3, 2024. Date of online publication: November 27, 2024.

This work was supported by Guangdong Basic and Applied Basic Research Foundation (No. 2022A1515240030) and Shenzhen Innovation & Entrepreneurship Program (No. JSGG20211029095544001).



N. Liu, H. Wang (corresponding author), and Y. Zhang are with the School of Mechanical Engineering and Automation, Harbin Institute of Technology, Shenzhen 518055, China (e-mail: liuni5739@outlook. com; hongwang@hit. edu. cn; 22s153253@stu.hit.edu.cn).

W. Zhou is with the Australian Energy Market Operator, Melbourne VIC 3000, Australia (e-mail: weihua.zhou@ieee.org).

J. Song and E. Prieto-Araujo are with Department of Electrical Engineering, Technical University of Catalonia, Barcelona 08028, Spain (e-mail: jie. song@upc.edu; eduardo.prieto-araujo@upc.edu).

Z. Chen is with the Department of Energy Technology, Aalborg University, Aalborg 9220, Denmark (e-mail: zch@et.aau.dk).

DOI: 10.35833/MPCE.2023.000842

## I. Introduction

THE global pursuit of a sustainable and low-carbon future places significant emphasis on renewable energy generation, driving consequential modifications in the operation, structure, and dynamics of power systems. A notable manifestation of these changes is the transition from synchronous generator-dominated dynamics to converter-dominated dynamics in power systems [1]. Regrettably, this change engenders the emergence of several unexpected power system oscillations in practical engineering for the converter-dominated power systems [2]. Consequently, the small-signal stability analysis of converter-dominated power system emerges as a critical research area. It is worth mentioning that the stability analysis mentioned below is all small-signal stability analysis.

Impedance analysis methods play a crucial role in identifying the underlying causes of oscillations in converter-dominated power systems, which effectively explore the intricate dynamics and interactions between converters and the grid, enabling the formulation of impedance models in various forms [3]. A classical and widely used impedance model is the $dq$-domain impedance/admittance model (abbreviated as $V$-$I$ impedance/admittance model in the following), which offers a more intuitive representation of the equipment control characteristics [3]. However, it is advised that these advantages of $dq$-domain impedance model do not extend to the stability analysis for grid-forming (GFM) converters, especially those with a single-loop structure [4]. The distinction arises from the fact that grid-following (GFL) converters directly control the DC component of voltage or current signals in the $dq$ frame while GFM converters regulate phasor quantities such as bus voltage magnitude and frequency. From a control structure perspective, the modeling of the GFM converter benefits from choosing the magnitude and phase of the voltage as the input signals and the active and reactive power as the output signals [5], [6]. The derivate transfer function matrix model is defined as the $P/Q$-$\theta/V$ model [6], referred to as the power-domain model in [7] and as the amplitude-phase model in [8]. Consequently, both the $V$-$I$ model [3], [9] and the $P/Q$-$\theta/V$ model [8] become valuable tools for evaluating the stability of grid-connected converters with equivalent results, including both GFL and

GFM converters.

Originally concentrated on single-converter grid-connected systems, the frequency-domain models based on impedance or transfer function models extend their applicability to systems with several converters in GFL and GFM control. Therefore, the circuit representation of the converters is determined by the current and voltage characteristics of the terminal [10]. GFL converters are typically modeled as current sources in parallel with *V-I* admittances, while converters with constant frequency and constant voltage control are commonly represented as voltage sources in series with *V-I* impedance [11]. To facilitate analysis, the whole system is divided into two subsystems at the selected node, following the equivalent circuit model. Then, the impedance of each subsystem is obtained by aggregating the impedance of individual components according to the circuit principle [12], [13]. It should be noted that the aggregation process may exhibit right-half-plane (RHP) poles, particularly when combining the GFL and GFM impedances.

The Bode plots and generalized Nyquist criterion (GNC) are used in [14]. The stability analysis for interconnected systems with RHP poles requires checking the open-loop RHP pole numbers in the subsystem, as discussed in [15] and [16]. One commonly used method is plotting the pole-zero map of the impedance transfer function. However, there are two major disadvantages. The process of solving the poles involves an initial conversion into Smith-McMillan form, adding an additional layer of complexity to the calculation [15], [16]. Moreover, if the transfer function is the measurement model/spectrum, the parameters of measurement model need to be confirmed through fitting. Although the RHP pole and zero numbers can be determined based on the magnitude slope change and the phase change in the Bode plots, the method in [14] only applies to single-input single-output nonminimum-phase systems. A sequential stability analysis is developed to avoid the emergence of RHP poles during the impedance aggregation process, which is started from low-level nodes [12]. An alternative method involves dividing the system into a non-passive subsystem and a passive subsystem. By embedding the impedance model of non-passive modules (e. g., converters) as diagonal elements in the transfer function matrices of a non-passive system, this method avoids the emergence of RHP poles induced by the impedance aggregation process [17], [18]. However, a crucial assumption in this method, which asserts the absence of RHP poles in their *V-I* models when each converter maintains self-stability, is not rigorously demonstrated in the current studies.

The GFL and GFM converters can be represented as equivalent power sources connected in series with $P/Q$-$\theta/V$ impedance or in parallel with $P/Q$-$\theta/V$ admittance [5], [8]. Currently, two stability analysis techniques are applied by utilizing these equivalent power sources: torque theoretical analysis [19], [20] and impedance-ratio stability criteria [6], [8]. The former aligns with the principles employed in modeling synchronous generators, only focusing on the grid synchronization dynamics under disturbances. In contrast, the latter aligns with the frequency-domain analysis theory, enabling more precise conclusions regarding stability assessment. However, based on the authors' knowledge, the application scope of the $P/Q$-$\theta/V$ modeling framework proposed in [6] is confined to multi-GFM grid-connected systems. The impedance modeling in [17] and [18] seems to be easily extendable to power systems with GFL and GFM converters. However, the method in [17] and [18] raises a similar question, as previously discussed, concerning the presence of RHP poles in the $P/Q$-$\theta/V$ model of the self-stable converter. In fact, as illustrated in [8], the *V-I* model of a stable GFL converter does not have RHP poles, whereas the $P/Q$-$\theta/V$ model has one RHP pole. Consequently, it becomes imperative to verify the existence of RHP poles in the non-passive subsystem when applying the $P/Q$-$\theta/V$ modeling framework to power systems with GFL and GFM converters.

To eliminate the need to check the RHP pole numbers in the non-passive subsystem, this study revisits the presence of RHP poles in self-stable converter as well as the adaptability of the frequency-domain model, and explores the hybrid frequency-domain modeling framework for the power system with GFL and GFM converters. The main contributions of this study can be summarized as follows.

1) This study contributes to clarifying the discrepancies between the *V-I* and $P/Q$-$\theta/V$ models in stability analysis, particularly rectifying the vague understanding regarding the pole numbers of the frequency-domain model of a self-stable equipment.

2) This study investigates the appropriate model selection, either the *V-I* or the $P/Q$-$\theta/V$ impedance/admittance model, for the stability analysis of converters in different control modes.

3) This study introduces a hybrid frequency-domain modeling framework and stability criteria for power systems with GFL and GFM converters. The frequency-domain model simplifies the stability analysis process by eliminating the need to check the RHP pole numbers in the non-passive subsystem.

The rest of this paper is organized as follows. Section II briefly introduces the system configuration and the frequency-domain models. Then, the circuit insights and discrepancy of frequency-domain models are discussed in Section III. Afterward, Section IV discusses the frequency-domain model applicability for converters with different control strategies. Section V presents the multi-converter parallel system. Finally, Section VI outlines the main conclusions.

## II. System Configuration and Frequency-domain Models

### A. System Configuration

Figure 1 illustrates the studied system with GFL and GFM converters, where PCC is short for the point of common coupling. These converters utilize a three-phase full-bridge inverter circuit, featuring a DC-side capacitor and an AC-side L filter, which serve to maintain a stable DC-link voltage and filter out the switching harmonics, respectively. Given that the GFL converter directly regulates its DC-side voltage and the GFM converter controls the output power, the DC-side circuits of the GFL and GFM converters can be simplified as an ideal current source in parallel with an admittance and ideal voltage source in series with an impedance, respectively. The converter is connected to the series-compensated grid with the equivalent resistance $R_g$, the equivalent inductance $L_g$, and the equivalent capacitance $C_g$ [21].

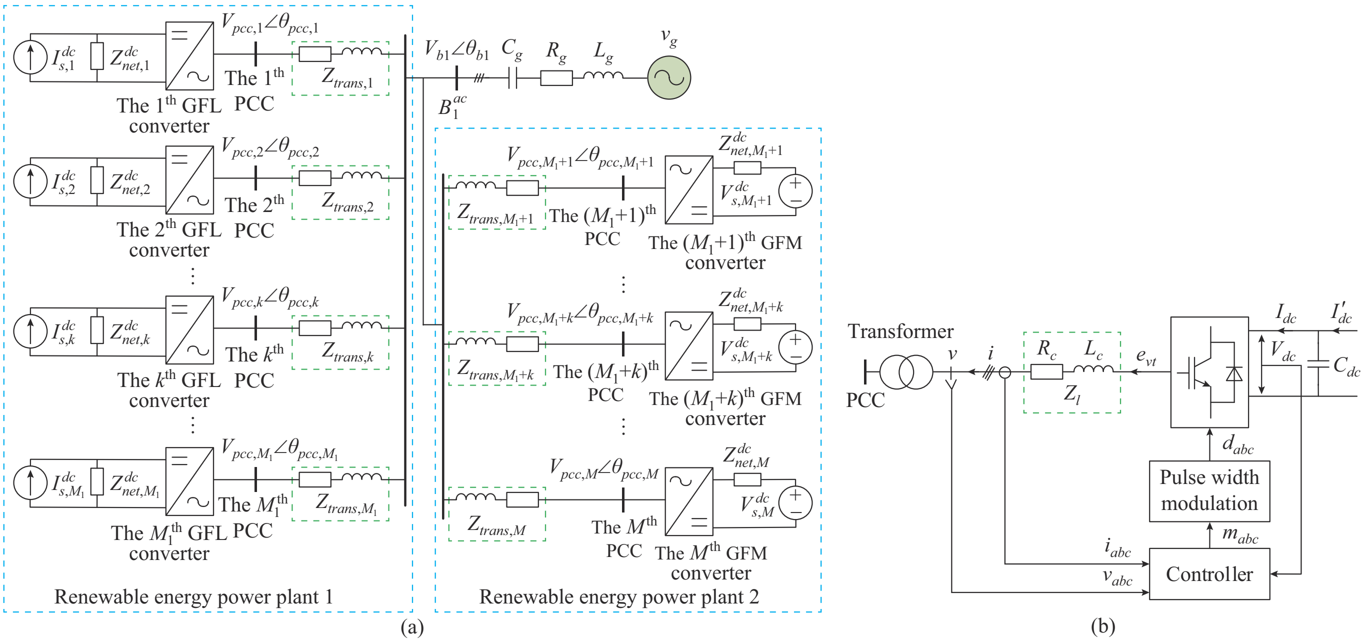


Fig. 1. Studied system with GFL and GFM converters. (a) Topology of studied system. (b) Topology of grid-connected converter.

It is worth mentioning that all the converters mentioned in this study are grid-connected voltage-source converters (VSCs). The common control structures of GFL and GFM converters are shown in Fig. 2, where PLL is short for the phase-locked loop. A GFL converter is designed to follow the grid voltage and frequency, adjusting the output power in response to changes in the grid voltage and frequency. The common control structure of a GFL converter is the two-loop cascaded control, as shown in Fig. 2(a). In contrast, the GFM converter does not require an external grid voltage reference, as it generates a stable voltage and frequency waveform that is synchronized with the grid. Figure 2(b) displays a common control structure of a GFM converter, where the power-based synchronization loop controller and the $Q$-$V$ droop controller generate the phase angle and magnitude of the terminal voltage of the GFM converter, respectively.

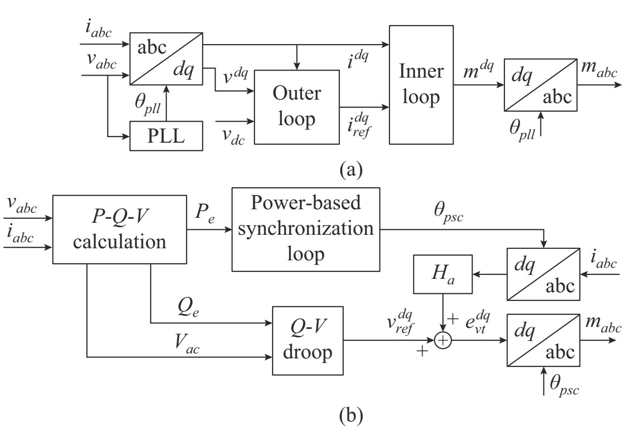


Fig. 2. Common control structures of GFL and GFM converters. (a) GFL converter. (b) GFM converter.

Figure 3 gives the control diagram of GFM converters. To suppress power resonance at approximately 50 Hz, a virtual resistance $H_a = R_a s/(s+\omega_b)$ is added to the output signal of $Q$-$V$ droop controller, where $R_a$ is the resistance; and $\omega_b$ is the cut-off frequency. The $Q$-$V$ droop controller consists of a proportional gain and a high-pass filter, with the high-pass filter typically set in the range of 0.1-0.2 p.u. for its cut-off frequency $\omega_b$, and the resistance $R_a$ chosen around 0.2 p.u. [22]. Notably, all GFM control structures aim to regulate the voltage amplitude and phase. The essential differences among these control structures are the voltage control at different positions (e.g., the GFM converter depicted in Fig. 3 controls the voltages at the converter switching bridge, while the GFM converter with multiple loops [9] regulates the voltages at the PCC) and the simulation of different reactive voltage equations.

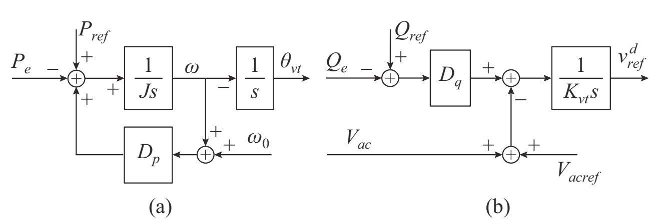


Fig. 3. Control diagram of GFM converters. (a) Power-based synchronization loop controller. (b) $Q$-$V$ droop controller.

Thus, although this study analyzes only two typical configurations, the presented tool can be adapted for other options of converter control implementation in different applications.

### *B. Frequency-domain Models*

#### *1) V-I Impedance Model*

To analyze the interaction between the converters and the grid, the existing studies usually use $\Delta \boldsymbol{i}^{dq}$ and $\Delta \boldsymbol{v}^{dq}$ as the input and output signals of the frequency-domain model, respectively, deriving a *V-I* impedance or admittance model of the converter. The *V-I* impedance model of the converter can accordingly be expressed as [3]:

$$\Delta \boldsymbol{v}^{dq} = \underbrace{\begin{bmatrix} Z^{dd} & Z^{dq} \\ Z^{qd} & Z^{qq} \end{bmatrix}}_{\boldsymbol{Z}^{dq}} \Delta \boldsymbol{i}^{dq} \tag{1}$$

where the superscripts $d$ and $q$ denote the $d$-axis and $q$-axis parameters, respectively; $Z$ is the impedance; and $\Delta$ denotes the small disturbance component of the signal.

#### *2) P/Q-θ/V Impedance Model*

To analyze the power-frequency dynamic characteristics and their interaction of the converters, the output active power $P_e$ and reactive power $Q_e$ are usually used as input signals. The amplitude $V_{ac}$ and phase (frequency) $\theta_{ac}$ of the voltage at converter switching bridge or PCC voltages are used as output signals [6], [8]. The $P/Q$-$\theta/V$ impedance model of the converter can be expressed as:

$$\underbrace{\begin{bmatrix} \Delta\theta_{ac} \\ \Delta V_{ac} \end{bmatrix}}_{\Delta \boldsymbol{V}^{\theta e}} = \underbrace{\begin{bmatrix} G^{\theta p} & G^{\theta q} \\ G^{ep} & G^{eq} \end{bmatrix}}_{\boldsymbol{Z}^{pq}} \underbrace{\begin{bmatrix} \Delta P_e \\ \Delta Q_e \end{bmatrix}}_{\Delta \boldsymbol{S}^{pq}} \tag{2}$$

where $G^{\theta p}$, $G^{\theta q}$, $G^{ep}$, and $G^{eq}$ are the elements of the equivalent impedance $\boldsymbol{Z}^{pq}$.

## III. Circuit Insights and Discrepancy of Frequency-domain Models

This section introduces the circuit insights and stability criteria based on different frequency-domain models. This section also studies the discrepancy of frequency-domain models of the converters and transmission lines.

### *A. Circuit Insights and Stability Criteria*

The relationship between the output power and the PCC voltage/current, as well as the relationship between the $dq$-axis voltage and the amplitude and phase of the voltage at the converter switching bridge, is given as [8]:

$$\begin{bmatrix} \Delta P_e \\ \Delta Q_e \end{bmatrix} = \underbrace{\begin{bmatrix} \overbrace{\begin{matrix} \frac{3}{2}I_0^d & \frac{3}{2}I_0^q \\ -\frac{3}{2}I_0^q & \frac{3}{2}I_0^d \end{matrix}}^{\boldsymbol{A}_V} & \overbrace{\begin{matrix} \frac{3}{2}V_0^d & \frac{3}{2}V_0^q \\ \frac{3}{2}V_0^q & -\frac{3}{2}V_0^d \end{matrix}}^{\boldsymbol{A}_I} \end{bmatrix}}_{\boldsymbol{T}_{PV}} \begin{bmatrix} \Delta \boldsymbol{v}^{dq} \\ \Delta \boldsymbol{i}^{dq} \end{bmatrix} \tag{3}$$

$$\Delta \boldsymbol{v}^{dq} = \underbrace{\begin{bmatrix} 0 & 1 \\ V_{ac0} & 0 \end{bmatrix}}_{\boldsymbol{T}_{\theta e}} \begin{bmatrix} \Delta\theta_{ac} \\ \Delta V_{ac} \end{bmatrix} = \boldsymbol{T}_{\theta e} \Delta \boldsymbol{V}^{\theta e} \tag{4}$$

where the subscript 0 denotes the steady-state value; and $I$ and $V$ denote the current and voltage, respectively.

Substituting (3) and (4) into (2), the mathematical equivalence of the converter and the two subsystems using the $P/Q$-$\theta/V$ model can be expressed as [6]:

$$\begin{cases} \boldsymbol{Z}_{vsc}^{dq} = \boldsymbol{T}_{\theta e}^{-1} [\boldsymbol{A}_V - \boldsymbol{A}_I (\boldsymbol{Z}_{vsc}^{dq})^{-1}]^{-1} \\ \boldsymbol{Z}_g^{dq} = \boldsymbol{T}_{\theta e}^{-1} [\boldsymbol{A}_V + \boldsymbol{A}_I (\boldsymbol{Z}_g^{dq})^{-1}]^{-1} \end{cases} \tag{5}$$

where the subscripts "*vsc*" and "*g*" denote the parameters associated with the converter and the grid, respectively. Similarly, if the converter employs GFL or GFM control, the subscript will change from "*vsc*" to "*gfl*" or "*gfm*".

Figure 4(a) shows the Norton equivalent model based on the *V-I* model of the grid-connected converter system. The PCC voltage based on the Norton equivalent model $\boldsymbol{v}^{dq}$ is derived as [23]:

$$\boldsymbol{v}^{dq} = \frac{\boldsymbol{v}_g^{dq} \boldsymbol{Z}_{vsc}^{dq} - \boldsymbol{G}_{vsc}^{dq} \boldsymbol{v}_{r,vsc}^{dq} \boldsymbol{Z}_g^{dq}}{\boldsymbol{E} + \boldsymbol{Z}_{vsc}^{dq} \boldsymbol{Y}_g^{dq}} \frac{1}{\boldsymbol{Z}_g^{dq}} = \frac{\boldsymbol{Y}_g^{dq} \boldsymbol{v}_g^{dq} - \boldsymbol{Y}_{vsc}^{dq} \boldsymbol{G}_{vsc}^{dq} \boldsymbol{v}_{r,vsc}^{dq}}{\boldsymbol{Y}_{vsc}^{dq} + \boldsymbol{Y}_g^{dq}} \tag{6}$$

where $\boldsymbol{v}_{r,vsc}^{dq}$ and $\boldsymbol{G}_{vsc}^{dq}$ are the reference voltage vector and closed-loop reference-to-output frequency-domain model of the converter, respectively; $\boldsymbol{Y}^{dq}$ is the equivalent admittance; and $\boldsymbol{E}$ is the identity matrix.

Following the Norton equivalent model and Ohm's law, Fig. 4(b) shows the Thevenin equivalent model 1 of the grid-connected converter system, where the controlled current source amplitude and admittance values are multiplied by a coefficient matrix $\boldsymbol{A}_I$. The PCC voltage based on the Thevenin equivalent model 1 can be expressed as:

$$\boldsymbol{v}^{dq} = \frac{\boldsymbol{A}_I \boldsymbol{Y}_g^{dq} \boldsymbol{v}_g^{dq} - (\boldsymbol{A}_I \boldsymbol{G}_{vsc}^{dq} \boldsymbol{Y}_{vsc}^{dq} \boldsymbol{v}_{r,vsc}^{dq})}{\boldsymbol{A}_I (\boldsymbol{Y}_g^{dq} + \boldsymbol{Y}_{vsc}^{dq})} = \frac{\boldsymbol{I}_{r,g}^{dq} - \boldsymbol{I}_{r,vsc}^{dq}}{\boldsymbol{A}_I (\boldsymbol{Y}_g^{dq} + \boldsymbol{Y}_{vsc}^{dq})} \tag{7}$$

where $\boldsymbol{I}_{r,g}^{dq} = \boldsymbol{A}_I \boldsymbol{Y}_g^{dq} \boldsymbol{v}_g^{dq}$ and $\boldsymbol{I}_{r,vsc}^{dq} = \boldsymbol{A}_I \boldsymbol{G}_{vsc}^{dq} \boldsymbol{Y}_{vsc}^{dq} \boldsymbol{v}_{r,vsc}^{dq}$ are the reference amplitude vectors of the equivalent current sources on grid and converter sides, respectively.

Subsequently, the Thevenin equivalent model 2 is obtained by adjusting the equivalent admittance of two subsystems with a coefficient matrix $\boldsymbol{A}_V$, as shown in Fig. 4(c). The PCC voltage based on the Thevenin equivalent model 2 can be expressed as:

$$\boldsymbol{v}^{dq} = \frac{\boldsymbol{I}_{r,g}^{dq} - \boldsymbol{I}_{r,vsc}^{dq}}{(\boldsymbol{A}_I \boldsymbol{Y}_g^{dq} + \boldsymbol{A}_V) - (\boldsymbol{A}_V - \boldsymbol{A}_I \boldsymbol{Y}_{vsc}^{dq})} \tag{8}$$

Then, the $P/Q$-$\theta/V$ model of the two subsystems can be calculated from the derived impedance models and frequency sweep models. By multiplying the left and right sides of (8) by the inverse matrix $\boldsymbol{T}_{\theta e}^{-1}$ and substituting it into the $P/Q$-$\theta/V$ model, the PCC voltage can be calculated as:

$$\boldsymbol{V}^{\theta e} = \frac{\boldsymbol{v}_{r,g}^{\theta e} - \boldsymbol{S}_{r,vsc}^{pq} \boldsymbol{Z}_g^{pq}}{\boldsymbol{E} - \boldsymbol{Z}_g^{pq} \boldsymbol{Y}_{vsc}^{pq}} \tag{9}$$

where $\boldsymbol{v}_{r,g}^{\theta e} = \boldsymbol{T}_{\theta e}^{-1} \boldsymbol{v}_{r,g}^{dq}$; and $\boldsymbol{S}_{r,vsc}^{pq} = \boldsymbol{A}_V \boldsymbol{v}_{r,g}^{dq} + \boldsymbol{I}_{r,vsc}^{dq}$.

Figure 4(d) shows the simplified equivalent circuit based on the $P/Q$-$\theta/V$ model. Notably, the PCC voltage dynamics and the stability of the grid-connected converter system based on these four equivalent circuits remain consistent. Since measurement data from the model can be used directly in the GNC, this criterion serves as a powerful and efficient tool in the stability analysis for the power systems [1]. On the basis of (6), (9), and GNC, it is straightforward to consider that the stability of the grid-connected converter system can be determined by examining the number of clockwise encirclements of the open-loop gain $\boldsymbol{L}_{sys}^{dq} = \boldsymbol{Z}_{vsc}^{dq} \boldsymbol{Y}_g^{dq}$ or $\boldsymbol{L}_{sys}^{pq} = -\boldsymbol{Z}_g^{pq} \boldsymbol{Y}_{vsc}^{pq}$ around the point (−1, j0) [3]. However, it is essential to assume that frequency-domain models for apparatus do not exhibit RHP poles. This assumption results in discrepancies when using the GNC based on $P/Q$-$\theta/V$ models compared to impedance models. These discrepancies are illustrated later.

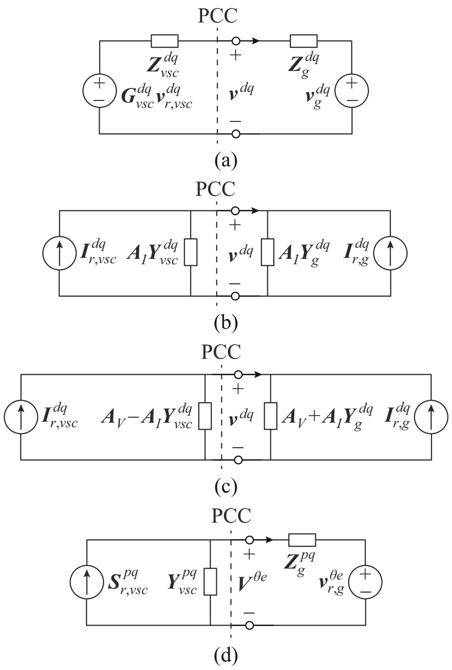


Fig. 4. Equivalent circuit model of grid-connected converter system. (a) Norton equivalent model based on *V-I* model. (b) Thevenin equivalent model 1. (c) Thevenin equivalent model 2. (d) Simplified equivalent circuit based on $P/Q$-$\theta/V$ model.

### *B. Discrepancy Between Frequency-domain Models*

#### *1) Frequency-domain Models of Converters*

Generally, the mathematical description of the converter typically comprises two components: the controller and the filter circuit. Neglecting the DC-side dynamics and switching losses of the converter, the output pulse width modulation signals of the control system can be approximately equal to the voltage at the switching bridge of the converter $\boldsymbol{e}_{vt}^{dq}$. That is to say,, the output signal of the control system is $\boldsymbol{e}_{vt}^{dq}$, which must be one of the input signals of the converter filter circuit. The state-space models of the two components can be expressed as:

$$\begin{cases}\dot{\boldsymbol{x}}_{ctrl}=\boldsymbol{F}_{ctrl}\boldsymbol{x}_{ctrl}+\boldsymbol{H}_{ctrl}\boldsymbol{a}_{ctrl}\\ \Delta\boldsymbol{e}_{vt}^{dq}=\boldsymbol{J}_{ctrl}\boldsymbol{x}_{ctrl}+\boldsymbol{K}_{ctrl}\boldsymbol{a}_{ctrl}\end{cases} \tag{10}$$

$$\begin{cases}\dot{\boldsymbol{x}}_{filter}=\boldsymbol{F}_{filter}\boldsymbol{x}_{filter}+\boldsymbol{H}_{filter}\boldsymbol{a}_{filter}\\ \boldsymbol{b}_{filter}=\boldsymbol{J}_{filter}\boldsymbol{x}_{filter}+\boldsymbol{K}_{filter}\boldsymbol{a}_{filter}\end{cases} \tag{11}$$

where $\boldsymbol{F}$, $\boldsymbol{H}$, $\boldsymbol{J}$, and $\boldsymbol{K}$ are the diagonal parameter matrices in the state-space representation of modules; $\boldsymbol{x}$, $\boldsymbol{a}$, and $\boldsymbol{b}$ are the state variables, input signals, and output signals, respectively; and the subscripts *ctrl* and *filter* represent the controller module and filter circuit module, respectively.

Moreover, the interconnection between the input signal and output signal of the composite system and the input/output signals of each module can be expressed by the algebraic equations as:

$$\begin{bmatrix}\boldsymbol{a}_{ctrl}\\ \boldsymbol{a}_{filter}\end{bmatrix}=\boldsymbol{L}_1\begin{bmatrix}\Delta\boldsymbol{e}_{vt}^{dq}\\ \boldsymbol{b}_{filter}\end{bmatrix}+\boldsymbol{L}_2\boldsymbol{u}_{vsc} \tag{12}$$

$$\boldsymbol{y}_{vsc}=\boldsymbol{L}_3\begin{bmatrix}\Delta\boldsymbol{e}_{vt}^{dq}\\ \boldsymbol{b}_{filter}\end{bmatrix}+\boldsymbol{L}_4\begin{bmatrix}\boldsymbol{a}_{ctrl}\\ \boldsymbol{a}_{filter}\end{bmatrix} \tag{13}$$

where $\boldsymbol{u}_{vsc}$ and $\boldsymbol{y}_{vsc}$ are the input and output signals for the converters of the composite system, respectively; and $\boldsymbol{L}_1$, $\boldsymbol{L}_2$, $\boldsymbol{L}_3$, and $\boldsymbol{L}_4$ are the parameter matrices that map the interconnection relationships among different components.

Then, according to the component connection-based modular state-space modeling method in [24] and the relationship between the state-space model and the frequency-domain model, the overall state-space model and frequency-domain model of the converter can be expressed as:

$$\begin{cases}\dot{\boldsymbol{x}}_{vsc}=\boldsymbol{A}_{vsc}\boldsymbol{x}_{vsc}+\boldsymbol{B}_{vsc}\boldsymbol{u}_{vsc}\\ \boldsymbol{y}_{vsc}=\boldsymbol{C}_{vsc}\boldsymbol{x}_{vsc}+\boldsymbol{D}_{vsc}\boldsymbol{u}_{vsc}\end{cases} \tag{14}$$

$$\boldsymbol{G}_{vsc}=\frac{\boldsymbol{y}_{vsc}}{\boldsymbol{u}_{vsc}}=\boldsymbol{C}_{vsc}(s\boldsymbol{E}-\boldsymbol{A}_{vsc})^{-1}\boldsymbol{B}_{vsc}+\boldsymbol{D}_{vsc} \tag{15}$$

where $\boldsymbol{A}_{vsc}=\boldsymbol{F}_{vsc}+\boldsymbol{H}_{vsc}\boldsymbol{L}_1(\boldsymbol{E}-\boldsymbol{K}_{vsc}\boldsymbol{L}_1)^{-1}\boldsymbol{J}_{vsc}$ is the parameter matrix, and $\boldsymbol{F}_{vsc}$, $\boldsymbol{H}_{vsc}$, and $\boldsymbol{J}_{vsc}$ are the diagonal matrices with parameter matrices $\boldsymbol{F}$, $\boldsymbol{H}$, and $\boldsymbol{J}$ of submodule (control system and filter) as the diagonal elements; and $\boldsymbol{B}_{vsc}$, $\boldsymbol{C}_{vsc}$, and $\boldsymbol{D}_{vsc}$ are the the parameter matrices of the overall state-space model of the converter.

Equations (12) and (13) show that selecting different input or output signals of the composite system can result in changes to $\boldsymbol{L}_1$-$\boldsymbol{L}_4$. For $P/Q$-$\theta/V$ frequency-domain modeling, (12) can be rewritten as (16), where the parameter matrices are labeled with the superscripts "$pq$" and "$dq$". The former refers to selecting the output power $\Delta\boldsymbol{S}^{pq}$ and the amplitude and phase of the voltage $\Delta\boldsymbol{V}^{\theta e}$ as input and output signals, respectively, while the latter refers to selecting the corresponding $dq$-axis voltage $\boldsymbol{v}^{dq}$ and $dq$-axis current $\boldsymbol{i}^{dq}$ as input and output signals, respectively.

$$\begin{bmatrix}\boldsymbol{a}_{ctrl}\\ \boldsymbol{a}_{filter}\end{bmatrix}=\boldsymbol{L}_1^{pq}\begin{bmatrix}\Delta\boldsymbol{e}_{vt}^{dq}\\ \boldsymbol{b}_{filter}\end{bmatrix}+\underbrace{\begin{bmatrix}\boldsymbol{L}_2^{11,pq} & \boldsymbol{L}_2^{12,pq}\\ \boldsymbol{L}_2^{21,pq} & \boldsymbol{L}_2^{22,pq}\end{bmatrix}}_{\boldsymbol{L}_2^{pq}}\begin{bmatrix}\Delta P_e\\ \Delta Q_e\end{bmatrix} \tag{16}$$

Then, substituting (3) into (16) yields:

$$\begin{aligned}\begin{bmatrix}\boldsymbol{a}_{ctrl}\\ \boldsymbol{a}_{filter}\end{bmatrix}=&\begin{bmatrix}\boldsymbol{L}_2^{11,pq} & \boldsymbol{L}_2^{12,pq}\\ \boldsymbol{L}_2^{21,pq} & \boldsymbol{L}_2^{22,pq}\end{bmatrix}\boldsymbol{A}_V\Delta\boldsymbol{v}^{dq}+\\ &\begin{bmatrix}\boldsymbol{L}_2^{11,pq} & \boldsymbol{L}_2^{12,pq}\\ \boldsymbol{L}_2^{21,pq} & \boldsymbol{L}_2^{22,pq}\end{bmatrix}\boldsymbol{A}_I\Delta\boldsymbol{i}^{dq}+\boldsymbol{L}_1^{pq}\begin{bmatrix}\Delta\boldsymbol{e}_{vt}^{dq}\\ \boldsymbol{b}_{filter}\end{bmatrix}\end{aligned} \tag{17}$$

Selecting the input signal in *V-I* model as the voltage $\boldsymbol{v}^{dq}$, the output signal $\boldsymbol{i}^{dq}$ can be expressed in a linear form related to $\boldsymbol{b}_{filter}$, namely $\boldsymbol{i}^{dq}=\boldsymbol{L}_b\boldsymbol{b}_{filter}$. Then, the relationship between $\boldsymbol{L}_1^{dq}$ in the *V-I* model and $\boldsymbol{L}_1^{pq}$ in the $P/Q$-$\theta/V$ model is:

$$\boldsymbol{L}_1^{dq}=\boldsymbol{L}_1^{pq}+\underbrace{\begin{bmatrix}\boldsymbol{0} & \boldsymbol{L}_2^{pq}\boldsymbol{A}_I\boldsymbol{L}_b\end{bmatrix}}_{\Delta\boldsymbol{L}_{mv}} \tag{18}$$

It is worth noting that the matrices $\boldsymbol{L}_1^{dq}$ and $\boldsymbol{L}_1^{pq}$ may not be equal, as indicated by (18). This implies that the parameter matrix $\boldsymbol{A}_{vsc}^{dq}$ is not necessarily equal to the parameter matrix $\boldsymbol{A}_{vsc}^{pq}$, because the matrices $\boldsymbol{F}_{vsc}$, $\boldsymbol{H}_{vsc}$, $\boldsymbol{K}_{vsc}$, and $\boldsymbol{J}_{vsc}$ are the same. This suggests that the absence of an RHP pole in one frequency-domain model does not guarantee the absence of an RHP pole in others, as zero-pole cancellation can occur in the frequency-domain model.

*2) Frequency-domain Models of Grid*

The dynamic equations of the grid with inductor $L_g$ and resistance $R_g$ in $dq$ frame can be given as:

$$\Delta \boldsymbol{v}_g^{dq} = \Delta \boldsymbol{v}^{dq} - \underbrace{\begin{bmatrix} R_g + sL_g & \omega_0 L_g \\ -\omega_0 L_g & R_g + sL_g \end{bmatrix}}_{\boldsymbol{Z}_g^{dq}} \Delta \boldsymbol{i}^{dq} \tag{19}$$

where $\omega_0$ is the rated angular velocity of the grid.

Substituting (19) and (4) into (3) to eliminate the variables $\Delta \boldsymbol{v}^{dq}$ and $\Delta \boldsymbol{i}^{dq}$, the relationship among the transmission power and the voltages at two ends can be given as:

$$\begin{bmatrix} \Delta P_e \\ \Delta Q_e \end{bmatrix} = \boldsymbol{Y}_g^{pq} \begin{bmatrix} \Delta \theta_{ac} \\ \Delta V_{ac} \end{bmatrix} - \boldsymbol{A}_I \boldsymbol{Y}_g^{dq} \begin{bmatrix} \Delta v_g^d \\ \Delta v_g^q \end{bmatrix} \tag{20}$$

$$\boldsymbol{Y}_g^{pq} = \begin{bmatrix} -Q_{e0} + \dfrac{1.5 V_{ac0}^2 \omega_0 L_g}{K_g} & \dfrac{P_{e0}}{V_{ac0}} + \dfrac{1.5 V_{ac0} (R_g + sL_g)}{K_g} \\ P_{e0} - \dfrac{1.5 V_{ac0}^2 (R_g + sL_g)}{K_g} & \dfrac{Q_{e0}}{V_{ac0}} + \dfrac{1.5 \omega_0 L_g V_{ac0}}{K_g} \end{bmatrix} \tag{21}$$

$$\boldsymbol{Z}_g^{pq} = \begin{bmatrix} \dfrac{F_2}{F_1} & \dfrac{F_3}{F_1} \\ \dfrac{F_4}{F_1} & \dfrac{F_5}{F_1} \end{bmatrix} \tag{22}$$

where $K_g = (R_g + sL_g)^2 + (\omega_0 L_g)^2$; $F_1 = K_g^2 (P_{e0}^2 + Q_{e0}^2) + V_{ac0}^4 \cdot [4.5 s L_g R_g - 2.25 R_g^2 + L_g^2 (-2.25 s^2 - 2.25 \omega_0^2)]$; and the coefficients $F_2$, $F_3$, $F_4$, and $F_5$ are given in Appendix A.

From (19), (21), and (22), the frequency-domain models $\boldsymbol{Z}_g^{dq}$, $\boldsymbol{Y}_g^{dq}$, and $\boldsymbol{Y}_g^{pq}$ do not exhibit RHP poles as the poles of $\boldsymbol{Y}_g^{dq}$ and $\boldsymbol{Y}_g^{pq}$ are $-R_g/L_g$. The RHP poles of $\boldsymbol{Z}_g^{pq}$ can be obtained by solving $F_1 = 0$. From (A6)-(A9) in Appendix A, it is observed that the $P/Q$-$\theta/V$ impedance model exhibits one RHP pole when $9V_0^4 - 4X_g^2 P_{e0}^2 - 4X_g^2 Q_{e0}^2 - 4P_{e0}^2 R_{g0}^2 > 0$. The steady-state operating point is set with $V_0 = 1$ p.u., $P_{e0} = 1$ p.u., $Q_{e0} = 0$ p.u., and $X_g$ and $R_g$ are usually less than 1 p.u., which is easily satisfied in practice. Therefore, the $P/Q$-$\theta/V$ impedance model $\boldsymbol{Z}_g^{pq}$ of the grid has one RHP pole, which highlights that different model forms of the grid may have discrepancies in their RHP poles. Even for a stable equipment, one model may have RHP poles, whereas the other models may not.

To conclude, both the $V$-$I$ model and the $P/Q$-$\theta/V$ model are utilized in the stability analysis for grid-connected converter systems. While the utilization of these models for assessing the stability of the entire closed loop yields consistent results, there may be discrepancies in how accurately different frequency-domain models describe the physical properties of a system. It is crucial to recognize that not all models can accurately reflect the self-stability nature of the apparatus. Improper choice of the model results in an additional step in the stability analysis, requiring the examination of RHP poles of the open-loop gain matrices.

## IV. Frequency-domain Model Applicability for Converters with Different Control Strategies

This section focuses on the selection of the appropriate frequency-domain model of the converter in stability analysis based on its design model. Two cases are given to illustrate the rationality of the frequency-domain model.

### *A. Frequency-domain Model Applicability of GFL Converters in Stability Analysis*

By using the current decoupling control and neglecting the dynamics of PLL, the $d$-axis closed-loop frequency-domain model of GFL converters with a proportional-integral (PI) inner controller $G_{vcc}(s) = k_{pc} + k_{pi}/s$ and a filter circuit $G_{filter}(s) = 1/(L_c s)$ is given as [25]:

$$\Delta i^d = \underbrace{\frac{k_{pc} s + k_{pi}}{L_c s^2 + k_{pc} s + k_{pi}}}_{G_{inner}^d(s)} \Delta i_{ref}^d + \underbrace{\frac{s}{L_c s^2 + k_{pc} s + k_{pi}}}_{Y_{inner}^{dd}(s)} \Delta v^d \tag{23}$$

where $i_{ref}^d$ is the $d$-axis component of the desired current; and $L_c$ is the filter inductance.

Similarly, the $q$-axis frequency-domain model $Y_{inner}^{qq}(s)$ can be obtained. Obviously, the design model of GFL converter involves a frequency-domain model with current as the input signal and voltage as the output signal. Furthermore, during the design process of the converter, both frequency-domain models $Y_{inner}^{dd}$ and $Y_{inner}^{qq}$ are ensured to be free of RHP poles and exhibit a certain stability margin. Considering that the design model can be considered as a $V$-$I$ admittance model that neglects the dynamics of PLL, it is anticipated that the $V$-$I$ admittance model $\boldsymbol{Y}_{gfl}^{dq}$ of the GFL converter does not possess any RHP poles. However, it is worth mentioning that there is no absolute guarantee that the $V$-$I$ admittance model $\boldsymbol{Y}_{gfl}^{dq}$ of the converter is completely free of RHP poles, especially under non-unity power factor conditions. Fortunately, the converter parameters are optimized through a trial-and-error process to ensure the self-stability of the converter. In contrast to the $P/Q$-$\theta/V$ model, which is not involved during the design process of the converter, it is more reasonable that the self-stability of the converter implies the absence of RHP poles in the $V$-$I$ admittance model of the GFL converters.

Thus, a more appropriate approach for assessing the stability is to model the GFL converter as an ideal current source in parallel with the $V$-$I$ admittance model. The stability analysis cases for GFL converters in [8] provide proof. The calculation results in [8] illustrate that the impedance model of a stable GFL converter does not have RHP poles, but the $P/Q$-$\theta/V$ model may have RHP poles.

### *B. Frequency-domain Model Applicability of GFM Converters in Stability Analysis*

The converter under the GFM control is given as:

$$\begin{cases} P_{ref} - P_e + D_p(\omega_0 - \omega) = J_{vt} \dfrac{\mathrm{d}\omega}{\mathrm{d}t} \\ D_q(Q_{ref} - Q_e) + V_{ac} - V_{acref} = K_{vt} \dfrac{\mathrm{d}E_{vt}}{\mathrm{d}t} \\ \theta_{vt} = \displaystyle\int \omega \, \mathrm{d}t \end{cases} \tag{24}$$

where $J_{vt}$ and $K_{vt}$ are the inertias of active power loop and reactive power loop, respectively; $D_p$ and $D_q$ are the active droop coefficient and the reactive droop coefficient, respectively; $E_{vt}\angle\theta_{vt}$ is the PCC voltage phasor; and $P_{ref}$, $Q_{ref}$, and

$V_{acref}$ are the active power reference, the reactive power reference, and the rated root mean square value of the PCC voltage, respectively.

Assuming that the grid is inductive, the inductive component $X_t = \omega_0 (L_c + L_g)$ of the converter filter and grid inductor is significantly larger than the resistance component $R_c + R_g$. Thus, we can neglect the resistance component. Disregarding the transmission line dynamics and the power coupling term [26], the model of the GFM converters can be obtained by substituting (24) into (20).

$$\begin{cases} \Delta P_e = \underbrace{\frac{3V_g E_{vt}}{X_t} \frac{1}{J_{vt}s + D_p} \frac{1}{s}}_{G_{p,open}(s)} (\Delta P_{ref} - \Delta P_e) - \frac{3V_g \delta_{vt0}}{X_t} \Delta V_g \\ \Delta Q_e = \underbrace{\frac{3E_{vt}}{X_t} \frac{D_q}{K_{vt}s + 1}}_{G_{q,open}(s)} (\Delta Q_{ref} - \Delta Q_e) - \frac{3E_{vt}}{X_t} \Delta V_g \end{cases} \tag{25}$$

where $\delta_{vt0}$ is the power angle between the converter voltage and the grid voltage.

Therefore, the closed-loop transfer functions of the active power loop $G_{p,close}(s)$ and reactive power loop $G_{q,close}(s)$ can be easily expressed as:

$$\begin{cases} \Delta P_e = \frac{G_{p,open}(s)}{1 + G_{p,open}(s)} \Delta P_{ref} - \frac{\frac{3V_g \delta_{vt}}{X_t}}{1 + G_{p,open}(s)} \Delta V_g \\ \Delta Q_e = \frac{G_{q,open}(s)}{1 + G_{q,open}(s)} \Delta Q_{ref} - \frac{\frac{3E_{vt}}{X_t}}{1 + G_{q,open}(s)} \Delta V_g \end{cases} \tag{26}$$

In contrast to the GFL converter, the parameter tuning model (26) of the GFM converters does choose output power and the magnitude/phase of the PCC voltage as input/output signals [26]. During the design process of the GFM converter, the zeros of $1+G_{p,open}(s)$ and $1+G_{q,open}(s)$ are placed in the left-half plane by analyzing the Bode diagrams of the open-loop transfer functions $G_{p,open}(s)$ and $G_{q,open}(s)$, respectively. Thus, the design model of GFM converters can be considered as a *P*/*Q*-*θ*/*V* model that ignores the dynamics of inductance, transmission line resistance, filter resistance, and power coupling. Furthermore, the design model of GFM converters considers grid impedance, but it is not presented in the *P*/*Q*-*θ*/*V* model. With the consideration of the stability margin and trial-and-error process in parameter tuning, it is reasonable to assume that the *P*/*Q*-*θ*/*V* model of GFM converters does not have RHP poles. In contrast, the RHP pole numbers in the *V*-*I* model are uncertain since they are not involved in the design process of the GFM converter. One stable case and one unstable case are provided in the next subsection, which also prove this inference.

### C. Cases Analysis for GFM Converters

Figure 5 shows the Bode diagram of $G_{q,open}(s)$ and $G_{p,open}(s)$ of the GFM converter, utilizing the simulation parameters provided in Table I.

For an active power loop, the crossover frequency is 14.6 Hz, the phase margin is 28.5°, and the magnitude of the active power loop gain at 100 Hz is −32.4 dB (which corresponds to 0.0239).

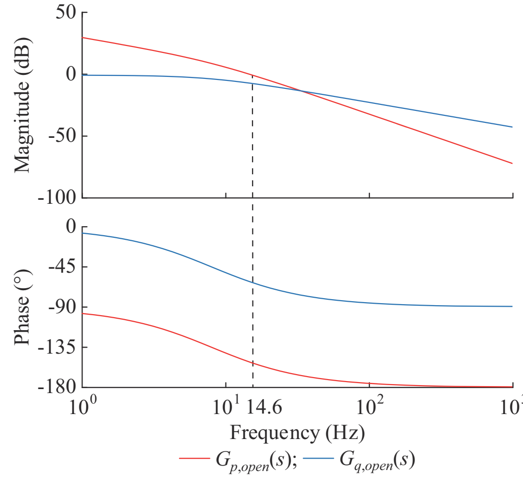


Fig. 5. Bode diagram of $G_{p,open}(s)$ and $G_{q,open}(s)$.

TABLE I
SIMULATION PARAMETERS

| Module | Parameter | Symbol | Value |
|---|---|---|---|
| Filter circuit | Rated power | $S_{gfl}$, $S_{gfm}$ | 2 MW, 2 MW |
| | Rated frequency | $f_0$ | 50 Hz |
| | Transformer ratio | $K_{rans}$ | 66 kV/690 V |
| | Equivalent inductance and resistance of grid | $L_g$, $R_g$ | 0.2 p.u., 0.02 p.u. |
| | Filter inductance, capacitance, and resistance | $L_c$, $C_c$, $R_c$ | 26.3 mH, 40 μF, 0.5 mΩ |
| Controller | Vector current controller | $k_{pc,g}$, $k_{ic,g}$ | 0.33, 0.6283 |
| | Direct-voltage controller | $k_{pdc,g}$, $k_{idc,g}$ | 1.47, 132 |
| | PLL | $k_{ppll,g}$, $k_{ipll,g}$ | 40, 800 |
| | Inertia of active power loop and active droop coefficient | $J_{vt}$, $D_p$ | 0.02, 0.02 |
| | Inertia of reactive power loop and reactive droop coefficient | $K_{vt}$, $D_q$ | 0.02, 0.20 |

In addition, the magnitude of the reactive power loop gain at 100 Hz is −22.5 dB (which corresponds to 0.0749). Therefore, the amplitude margin and the phase margin of the active power loop and the reactive power loop satisfy the required specifications, and the GFM converter is deemed self-stable [26]. To validate the above-mentioned conclusion, the stability of GFM converter is assessed by employing $\boldsymbol{L}_{sys}^{dq}$ and $\boldsymbol{L}_{sys}^{pq}$, considering the transition of the grid condition from an inductive grid to a series-compensated grid. The *V*-*I* model and *P*/*Q*-*θ*/*V* model of the converter are previously established in [27] and [5], respectively, and are not reiterated here.

*1) V-I Impedance Model*

Set the series compensation level (SCL) $SCL = 1/(\omega_0^2 L_g C_g)$ as 36% and 60%, respectively. In Fig. 6, $\lambda_1$ and $\lambda_2$ are the eigenvalues of $\boldsymbol{L}_{sys}^{dq}$. In both Fig. 6(a) and (b), the blue Nyquist curves do not encircle the point $(-1, \mathrm{j}0)$. However, in Fig. 6 (a) and (b), the red Nyquist curves encircle the point $(-1, \mathrm{j}0)$ once in clockwise and counterclockwise directions, respectively. This indicates that the encirclement number $N_{sys}$ of the point $(-1, \mathrm{j}0)$ for two cases is 1 and −1, respectively. With the common assumption that $\boldsymbol{Z}_{gfm}^{dq}$, $\boldsymbol{Y}_{g}^{dq}$, and $\boldsymbol{Z}_{g}^{dq}$ do not have

RHP poles, as illustrated in Section III-B, the grid-connected converter system has instability, while the grid-connected converter system with $SCL=60\%$ loses stability with one RHP pole.

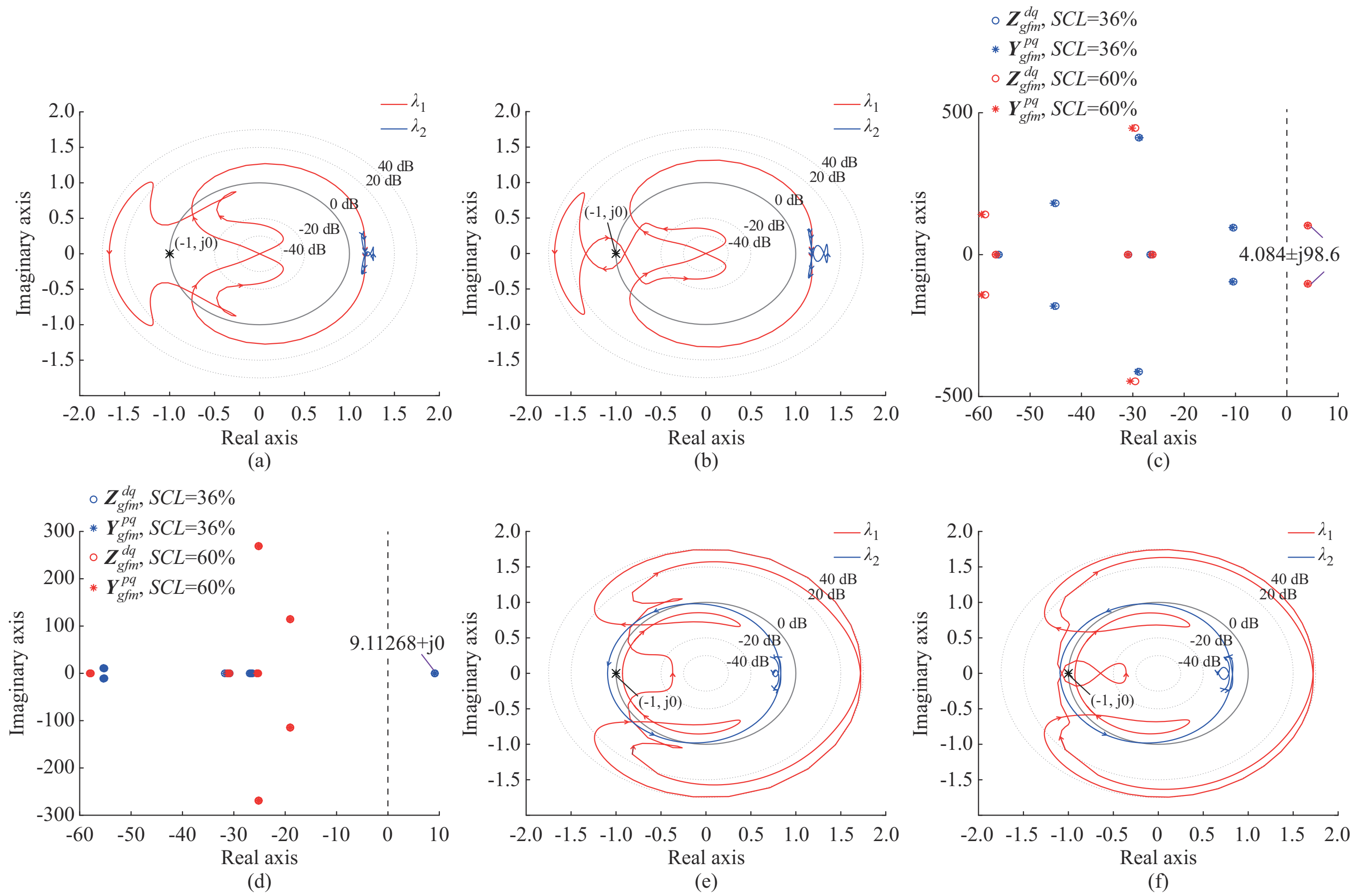


Fig. 6. Nyquist curves using *V-I* model $\boldsymbol{Z}_{gfm}^{dq}$ and *P*/*Q*-*θ*/*V* model $\boldsymbol{Y}_{gfm}^{dq}$, pole distribution, and eigenvalue distribution. (a) Nyquist curves of $\boldsymbol{Z}_{gfm}^{dq}$ when $SCL=36\%$. (b) Nyquist curves of $\boldsymbol{Z}_{gfm}^{dq}$ when $SCL=60\%$. (c) Eigenvalue distribution of closed-loop system. (d) Pole distribution of $\boldsymbol{Z}_{gfm}^{dq}$ and $\boldsymbol{Y}_{gfm}^{pq}$ of GFM converter. (e) Nyquist curves of $\boldsymbol{Y}_{gfm}^{pq}$ when $SCL=36\%$. (f) Nyquist curves of $\boldsymbol{Y}_{gfm}^{pq}$ when $SCL=60\%$.

However, by examining the eigenvalue distribution of the closed-loop system shown in Fig. 6(c), it is evident that the closed-loop system remains stable when $SCL=36\%$, whereas the closed-loop system exhibits instability with two RHP poles when *SCL* increases to 60%. The conflicting conclusions arise from the assumption that the *V-I* model of a self-stable converter does not have any RHP pole, whereas there is actually one pole present in two cases, as observed from the pole distribution of the *V-I* model $\boldsymbol{Z}_{gfm}^{dq}$ of the GFM converter in Fig. 6(d). Taking into account the existence of one RHP pole in the converter, the conclusions obtained from GNC align with the eigenvalue distribution, as shown in Fig. 6(c). It should be noted that the discrepancy in the stability analysis conclusions arises because the encirclement number of the point $(-1, j0)$ in the two cases is one with positive and negative directions, respectively. In conclusion, it can be stated that the *V-I* model of a self-stable GFM converter cannot guarantee the absence of an RHP pole.

*2) P/Q-θ/V Admittance Model*

Figure 6(d) also gives the pole distribution of the *P*/*Q*-*θ*/*V* admittance model $\boldsymbol{Y}_{gfm}^{pq}$ of the GFM converter. It can be observed that whether *SCL*=36% or *SCL*=60%, the poles of the *P*/*Q*-*θ*/*V* admittance model for the GFM converter are located in the left-half plane. However, it should be noted that there is an RHP pole in the *P*/*Q*-*θ*/*V* impedance model $\boldsymbol{Z}_{g}^{pq}$ of the transmission grid, as mentioned in Section III-B. Thus, the open-loop gain $\boldsymbol{Y}_{gfm}^{pq}\boldsymbol{Z}_{g}^{pq}$ has one RHP pole.

Figure 6(e) and (f) shows the Nyquist curves of the two cases based on $\boldsymbol{L}_{sys}^{pq}$, respectively. In Fig. 6(e), the blue Nyquist curve encircles the point $(-1, j0)$ in counterclockwise direction once, which indicates stability. Figure 6(b) shows that the red Nyquist curve encircles the point $(-1, j0)$ in clockwise direction twice, while the blue Nyquist curve encircles the point $(-1, j0)$ in counterclockwise direction once. This indicates that the system loses stability with two RHP poles when $SCL=60\%$. The conclusion is consistent with that of the eigenvalue distribution shown in Fig. 6(c). Thus, it is essential to acknowledge the limitations of assuming that frequency-domain model of self-stable equipment does not have RHP poles. A more appropriate approach to assessing the grid-connected stability issues is to model the GFM converter as an ideal power source in parallel with the *P*/*Q*-*θ*/*V* admittance model.

To validate the stability analysis conclusion, the nonlinear model of a single-converter grid-connected system is built on the MATLAB/Simulink platform.

Figure 7 shows the three-phase output current and active power waveforms of the converter when $SCL=36\%$ and $SCL=60\%$, as well as the fast Fourier transform (FFT) results from the output current when $SCL=60\%$. The 35 Hz and 65 Hz oscillation components are observed in Fig. 7(c), which correspond to the oscillation frequency of $2\pi\times(50-35)=94.2$ rad/s and $2\pi\times(65-50)=94.2$ rad/s. This is consistent with the eigenvalue distribution in Fig. 6(c), where the two unstable poles of the closed-loop system are both $4.084\pm$ j98.6. Additionally, Fig. 6(c) confirms that the eigenvalue distribution of the closed-loop system, derived from both the *V-I* model and the *P*/*Q*-*θ*/*V* model, exhibits substantial consistency, corroborating the findings in [8].

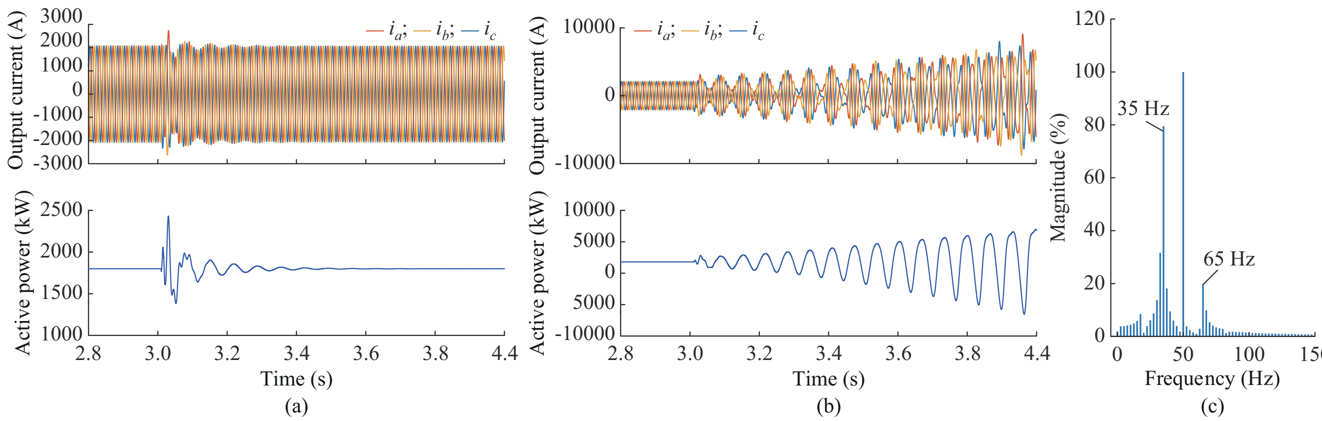


Fig. 7. Time-domain analysis results of single-converter grid-connected system. (a) Three-phase output current and active power waveforms of converter when $SCL=36\%$. (b) Three-phase output current and active power waveforms of converter when $SCL=60\%$. (c) FFT results from output current when $SCL=60\%$.

In summary, the utilization of different models during the design process of GFL and GFM converters leads to different interpretations of self-stability. For the GFL converter, self-stability implies the absence of RHP poles in the *V-I* admittance model, whereas the RHP pole number in the *P*/*Q*-*θ*/*V* model remains uncertain. Conversely, the self-stability in the GFM converter denotes the absence of an RHP pole in the *P*/*Q*-*θ*/*V* admittance model, while the pole in the *V-I* model may not possess this attribute. To reduce the complexity of the stability analysis, it is recommended that GFL converters are modeled as an ideal current source in parallel with the *V-I* admittance model, while GFM converters are modeled as an ideal power source in parallel with the *P*/*Q*-*θ*/*V* admittance model.

## V. Multi-converter Parallel System

This section presents a hybrid frequency-domain modeling framework and stability criteria for multi-converter parallel systems with the frequency-domain models of GFL and GFM converters built in the *V-I* and *P*/*Q*-*θ*/*V* models, respectively. The stability criteria are validated through a simulation case involving a studied system with both GFL and GFM converters.

### *A. Modeling Framework and Stability Criteria*

The assessment of the RPH pole number of the high-order transfer function matrix can be challenging, given the complexity involved in both calculating the poles of this matrix and identifying the parameters of the measurement model. The potential existence of RHP poles in the frequency-domain model of converter and the impedance aggregation process contribute to the emergence of RHP poles in the subsystem model. From the analysis in Section IV, it is evident that the *V-I* model of the GFM converter may exhibit RHP poles, resulting in an inaccurate conclusion. To address this, it is recommended to set the GFM converters as an ideal power source in parallel with the *P*/*Q*-*θ*/*V* admittance model. Subsequently, the *V-I* admittance of the GFL converter, the *P*/*Q*-*θ*/*V* admittance of the GFM converter, and the *V-I* impedance of the equivalent grid are embedded as diagonal elements in the transfer function matrices of the non-passive subsystem. In this modeling approach, each component in the non-passive system operates independently as an individual subsystem without interacting with other components. This ensures that the poles of the system models are the union of the poles of each submodule, thereby preventing the emergence of RHP poles during the impedance aggregation process.

Assuming each power plant shares the same control structure and parameters, each power plant is simplified and represented as a single equivalent source converter (ESC) using the capacity-weighted average method [28]. According to Fig. 4(a) and (b), the small-signal representation of the non-passive subsystem (including $M_1$ equivalent GFL converters, $M-M_1$ equivalent GFM converters, and the main grid) are expressed as:

$$\underbrace{\begin{bmatrix} \boldsymbol{i}_{cs}^{dq} \\ \boldsymbol{S}_{vs}^{pq} \\ \boldsymbol{v}_{b1}^{dq} \end{bmatrix}}_{\boldsymbol{X}_y} = \underbrace{\begin{bmatrix} \boldsymbol{G}_{cs}^{dq}\boldsymbol{i}_{r,cs}^{dq} \\ \boldsymbol{G}_{vs}^{pq}\boldsymbol{S}_{r,vs}^{pq} \\ \boldsymbol{v}_{g}^{dq} \end{bmatrix}}_{\boldsymbol{X}_r} - \boldsymbol{G}_{sld}^{HM} \underbrace{\begin{bmatrix} \boldsymbol{v}_{cs}^{dq} \\ \boldsymbol{V}_{vs}^{\theta e} \\ \boldsymbol{i}_{g}^{dq} \end{bmatrix}}_{\boldsymbol{X}_u} \tag{27}$$

where subscripts *cs* and *vs* denote the collective vectors or matrices of the equivalent GFL converter and the equivalent GFM converter, respectively; $\boldsymbol{v}_{b1}^{dq}$ is the *dq* component of the voltage at the point $B_1^{ac}$; and $\boldsymbol{G}_{sld}^{HM}$ is the transfer function matrix, which is a diagonal matrix with equipment admittances or impedances as diagonal elements, $\boldsymbol{G}_{sld}^{HM}=\mathrm{diag}(\boldsymbol{Y}_{gfl,1}^{dq},\boldsymbol{Y}_{gfl,2}^{dq},\ldots,\boldsymbol{Y}_{gfl,M_1}^{dq},\boldsymbol{Y}_{gfm,1}^{pq},\boldsymbol{Y}_{gfm,2}^{pq},\ldots,\boldsymbol{Y}_{gfm,M-M_1}^{pq},-\boldsymbol{Z}_g^{dq})$.

According to (20), the small-signal representation of transmission line from the $k^{\text{th}}$ equivalent GFM converter to the point $B_1^{ac}$ can be written as:

$$\Delta\boldsymbol{V}_{trans,k}^{\theta e}=\boldsymbol{Z}_{trans,k}^{pq}\Delta\boldsymbol{S}_{trans,k}^{pq}+\boldsymbol{G}_{trans,k}^{pq}\Delta\boldsymbol{v}_{b1}^{dq} \tag{28}$$

where $\Delta\boldsymbol{S}_{trans,k}^{pq}$ and $\Delta\boldsymbol{V}_{trans,k}^{\theta e}$ are the output vectors and disturbance vectors of the $k^{\text{th}}$ equivalent GFM converter, respectively; $\boldsymbol{Z}_{trans,k}^{pq}$ is the $P/Q$-$\theta/V$ model of the transmission line, which is given in (21); and $\boldsymbol{G}_{trans,k}^{pq}=\boldsymbol{Z}_{trans,k}^{pq}\boldsymbol{A}_I\boldsymbol{Y}_{trans,k}^{dq}$.

Substituting (19) into (3) to eliminate the variable $\boldsymbol{v}^{dq}$, the transmission line current from the $k^{\text{th}}$ equivalent GFM converter to the point $B_1^{ac}$ can be written as:

$$\Delta\boldsymbol{i}_{trans,k}^{dq}=\underbrace{(\boldsymbol{A}_V\boldsymbol{Z}_{trans,k}^{dq}+\boldsymbol{A}_I)^{-1}}_{\boldsymbol{G}_{trans,k}^{ip}}(\Delta\boldsymbol{S}_{trans,k}^{pq}-\boldsymbol{A}_V\Delta\boldsymbol{v}_{b1}^{dq}) \tag{29}$$

With respect to the topology shown in Fig. 1, the frequency-domain model of the passive subsystem (transmission line) can be reorganized as:

$$\begin{bmatrix}\boldsymbol{v}_{cs}^{dq}\\ \boldsymbol{V}_{vs}^{\theta e}\\ \boldsymbol{i}_g^{dq}\end{bmatrix}=\underbrace{\begin{bmatrix}\boldsymbol{Z}_{cs}^{dq} & \boldsymbol{0}_{2M_1\times2(M-M_1)} & \boldsymbol{E}_{2M_1\times2}\\ \boldsymbol{0}_{2(M-M_1)\times2M_1} & \boldsymbol{Z}_{vs}^{pq} & \boldsymbol{G}_{vs}^{b}\\ \boldsymbol{E}_{2\times2M_1} & \boldsymbol{G}_{vs}^{ip} & \boldsymbol{G}_{vs}^{iv}\end{bmatrix}}_{\boldsymbol{G}_{il}^{HM}}\begin{bmatrix}\boldsymbol{i}_{cs}^{dq}\\ \boldsymbol{S}_{vs}^{pq}\\ \boldsymbol{v}_{b1}^{dq}\end{bmatrix} \tag{30}$$

where $\boldsymbol{G}_{vs}^{iv}$ is the parameter matrix, which is obtained by summing $-\boldsymbol{G}_{trans,k}^{iv}\boldsymbol{A}_V$ for $k$ ranging from $M_1+1$ to $M$, namely $\boldsymbol{G}_{vs}^{iv}=-\sum_{k=M_1+1}^{M}\boldsymbol{G}_{trans,k}^{iv}\boldsymbol{A}_V$; and other parameters are given as:

$$\begin{cases}\boldsymbol{Z}_{cs}^{dq}=\mathrm{diag}(\boldsymbol{Z}_{trans,1}^{dq},\boldsymbol{Z}_{trans,2}^{dq},\ldots,\boldsymbol{Z}_{trans,M_1}^{dq})\\ \boldsymbol{Z}_{vs}^{pq}=\mathrm{diag}(\boldsymbol{Z}_{trans,M_1+1}^{pq},\boldsymbol{Z}_{trans,M_1+2}^{pq},\ldots,\boldsymbol{Z}_{trans,M}^{pq})\\ \boldsymbol{G}_{vs}^{b}=[\boldsymbol{G}_{trans,M_1+1}^{b},\boldsymbol{G}_{trans,M_1+2}^{b},\ldots,\boldsymbol{G}_{trans,M}^{b}]^{\mathrm{T}}\\ \boldsymbol{E}_{M_1}=[\boldsymbol{E}_{2\times2},\boldsymbol{E}_{2\times2},\ldots,\boldsymbol{E}_{2\times2}]^{\mathrm{T}}\\ \boldsymbol{G}_{vs}^{ip}=[\boldsymbol{G}_{trans,M_1+1}^{ip},\boldsymbol{G}_{trans,M_1+2}^{ip},\ldots,\boldsymbol{G}_{trans,M}^{ip}]^{\mathrm{T}}\end{cases} \tag{31}$$

Substituting (30) to (27), the closed-loop transfer function of the overall system can be written as:

$$\boldsymbol{X}_y=\frac{\boldsymbol{X}_r}{\boldsymbol{E}+\boldsymbol{G}_{sld}^{HM}\boldsymbol{G}_{il}^{HM}} \tag{32}$$

where $\boldsymbol{G}_{il}^{HM}$ is the transfer function matrix representing the small-signal dynamics of the interlinking line.

With the assumption that the converters remain self-stability without considering the grid dynamics, the transfer function matrix $\boldsymbol{G}_{sld}^{HM}$ is assumed to be free of RHP poles. However, the impedance matrix $\boldsymbol{G}_{il}^{HM}$ may contain RHP poles, as discussed in Section III-C. Therefore, the pole numbers of the system open-loop gain $\boldsymbol{L}_{sys}^{HM}=\boldsymbol{G}_{sld}^{HM}\boldsymbol{G}_{il}^{HM}$ equal the pole numbers $P_{il}^{HM}$ of $\boldsymbol{G}_{il}^{HM}$. If the encirclement number $N_{sys}$ of the system open-loop gain around the $(-1,\mathrm{j}0)$ point satisfies $N_{sys}-P_{il}^{HM}>0$, the system loses stability according to the GNC.

In Table II, the existence of RHP poles in the system open-loop gain is compared using the impedance aggregation model [13], the $V$-$I$ model [17], and the hybrid frequency-domain model proposed in this study. In contrast to the other two models, the hybrid frequency-domain model eliminates the requirements to check the RHP pole numbers in the model of the non-passive subsystem by ensuring that this model does not exhibit any RHP pole. Although the hybrid frequency-domain model still requires to check the presence of RHP poles in the passive system, it is considerably simpler than determining the RHP poles of the converter model. This can be attributed to the ease of obtaining line parameters and the lower order of the line model compared with the converter model.

TABLE II
COMPARISON OF THREE STABILITY ASSESSMENT MODELS

| Model | RPH pole in system open-loop gain |
|---|---|
| Impedance aggregation model [13] | Existence of RPH poles in system open-loop gain can stem from either converter itself or impedance aggregation process. RPH pole number in both subsystems must be checked before evaluating stability of power system. |
| $V$-$I$ model [17] | Emergence of RHP poles in system open-loop gain may arise from converter itself. Before evaluating stability of power system with GFL and GFM converters, it is essential to check RHP pole number in the model of non-passive subsystem. Such checks are not required for power systems exclusively employing GFL converters. |
| Hybrid frequency-domain model | There has no requirement to check presence of RPH poles in model of non-passive subsystem. For power system with GFL and GFM converters, it is crucial to check RPH pole number in model of passive subsystem. |

## B. Verification and Comparison

To verify the effectiveness and merit of the frequency-domain model, the stability analysis methods based on impedance aggregation model [13], the $V$-$I$ model [17], and hybrid frequency-domain model is utilized to assess the system stability, as illustrated in Fig. 1. The system configuration includes 50 GFL converter units and 50 GFM converter units, which are aggregated into a GFL converter and a GFM converter, respectively. The circuit and control parameters of the converter remain the same as those in Section IV-C. The resistance and inductance of the transmission line from ESC to point $B_1^{ac}$ are set to be 8.4 Ω and 2.6 mH, respectively.

Referring to [13], [17], and (27), the studied system can be evaluated by the system open-loop gains $\boldsymbol{L}_{sys}^{Agg}=\boldsymbol{Y}_{Agg}^{DQ}\boldsymbol{Z}_g^{dq}$, $\boldsymbol{L}_{sys}^{DQ}=\boldsymbol{G}_{sld}^{DQ}\boldsymbol{G}_{il}^{DQ}$, and $\boldsymbol{L}_{sys}^{HM}=\boldsymbol{G}_{sld}^{HM}\boldsymbol{G}_{il}^{HM}$, where the aggregate impedance $\boldsymbol{Y}_{Agg}^{DQ}$, the $V$-$I$ model $\boldsymbol{G}_{sld}^{DQ}$, and the hybrid model of the subsystem $\boldsymbol{G}_{sld}^{HM}$ are represented as:

$$\boldsymbol{Y}_{Agg}^{DQ}=\boldsymbol{Y}_{cs}^{dq}+\boldsymbol{Z}_{vs}^{dq} \tag{33}$$

$$\boldsymbol{G}_{sld}^{DQ}=\mathrm{diag}(\boldsymbol{Y}_{gfl,1}^{dq},\boldsymbol{Z}_{gfm,1}^{dq},-\boldsymbol{Z}_g^{dq}) \tag{34}$$

$$\boldsymbol{G}_{sld}^{HM}=\mathrm{diag}(\boldsymbol{Y}_{gfl,1}^{dq},\boldsymbol{Y}_{gfm,1}^{dq},-\boldsymbol{Z}_g^{dq}) \tag{35}$$

Therefore, $\boldsymbol{Y}_{cs}^{dq}$, $\boldsymbol{Y}_{vs}^{dq}$, and hybrid models $\boldsymbol{G}_{il}^{DQ}$ and $\boldsymbol{G}_{il}^{HM}$ of the transmission line can be written as:

$$\boldsymbol{Y}_{cs}^{dq}=(\boldsymbol{Z}_{gfl,1}^{dq}+\boldsymbol{Z}_{trans}^{dq})^{-1} \tag{36}$$

$$\boldsymbol{Y}_{vs}^{dq}=(\boldsymbol{Z}_{gfm,1}^{dq}+\boldsymbol{Z}_{trans})^{-1} \tag{37}$$

$$\boldsymbol{G}_{il}^{DQ}=\begin{bmatrix}\boldsymbol{Z}_{trans}^{dq} & \boldsymbol{0}_{2\times2} & \boldsymbol{E}_{2\times2}\\ \boldsymbol{0}_{2\times2} & \boldsymbol{Y}_{trans}^{dq} & -\boldsymbol{Y}_{trans}^{dq}\\ \boldsymbol{E}_{2\times2} & \boldsymbol{Y}_{trans}^{dq} & -\boldsymbol{Y}_{trans}^{dq}\end{bmatrix} \tag{38}$$

$$\boldsymbol{G}_{il}^{HM}=\begin{bmatrix}\boldsymbol{Z}_{trans}^{dq} & \boldsymbol{0}_{2\times2} & \boldsymbol{E}_{2\times2}\\ \boldsymbol{0}_{2\times2} & \boldsymbol{Z}_{trans}^{pq} & \boldsymbol{G}_{trans}^{b}\\ \boldsymbol{E}_{2\times2} & \boldsymbol{G}_{trans}^{ip} & -\boldsymbol{G}_{trans}^{ip}\boldsymbol{A}_{V}\end{bmatrix} \tag{39}$$

Figure 8(a) illustrates the pole distribution in the *V-I* model of equivalent GFL converter and equivalent GFM converter, as well as the *P*/*Q*-*θ*/*V* model of equivalent GFM converter. Only the pole of the *V-I* impedance model of the equivalent GFM converter is observed in the RHP, which aligns with the conclusion in Section IV. The pole distribution of the two subsystems is presented in Fig. 8(b), where $\boldsymbol{Y}_{Agg}^{DQ}$, $\boldsymbol{G}_{sld}^{DQ}$, and $\boldsymbol{G}_{il}^{HM}$ all have one RHP pole. It is evident that the pole of $\boldsymbol{G}_{sld}^{DQ}$ is introduced by the *V-I* model of equivalent GFM converter, while the pole of $\boldsymbol{G}_{il}^{HM}$ is introduced by the transmission line from equivalent GFM converter to point $B_1^{ac}$. It should be noted that, in these cases, the RHP pole in $\boldsymbol{Y}_{Agg}^{DQ}$ may be introduced by the impedance aggregation process or the RHP poles in the *V-I* model of the GFM converters. The case where the aggregation of GFL and GFM converters introduces RHP poles can be found in [15]. In addition, the results confirm that the *P*/*Q*-*θ*/*V* model of the non-passive subsystem does not exhibit RHP poles, while the *V-I* model does contain such poles.

Figure 9 shows the crucial Nyquist curves of $\boldsymbol{L}_{sys}^{Agg}$, $\boldsymbol{L}_{sys}^{DQ}$, and $\boldsymbol{L}_{sys}^{HM}$ when the grid switches from an inductive grid to a series-compensated grid with $SCL=63\%$. In Fig. 9, $\lambda_3$ and $\lambda_4$ are the eigenvalues of $\boldsymbol{L}_{sys}^{Agg}$. It should be reminded that this study omits the other Nyquist curves in Fig. 9(b) and (c) since none of them encircle the point $(-1, \mathrm{j}0)$. In Fig. 9(a) and (c), the Nyquist curve encircles the point $(-1, \mathrm{j}0)$ in clockwise direction once. Similarly, the Nyquist curve encircles the point $(-1, \mathrm{j}0)$ three times, twice clockwise and once counterclockwise in Fig. 9(b).

As each of the models $\boldsymbol{Y}_{Agg}^{DQ}$, $\boldsymbol{G}_{sld}^{DQ}$, and $\boldsymbol{G}_{il}^{HM}$ has one RHP pole, three models reach the same conclusion that the system loses stability with two RHP poles.

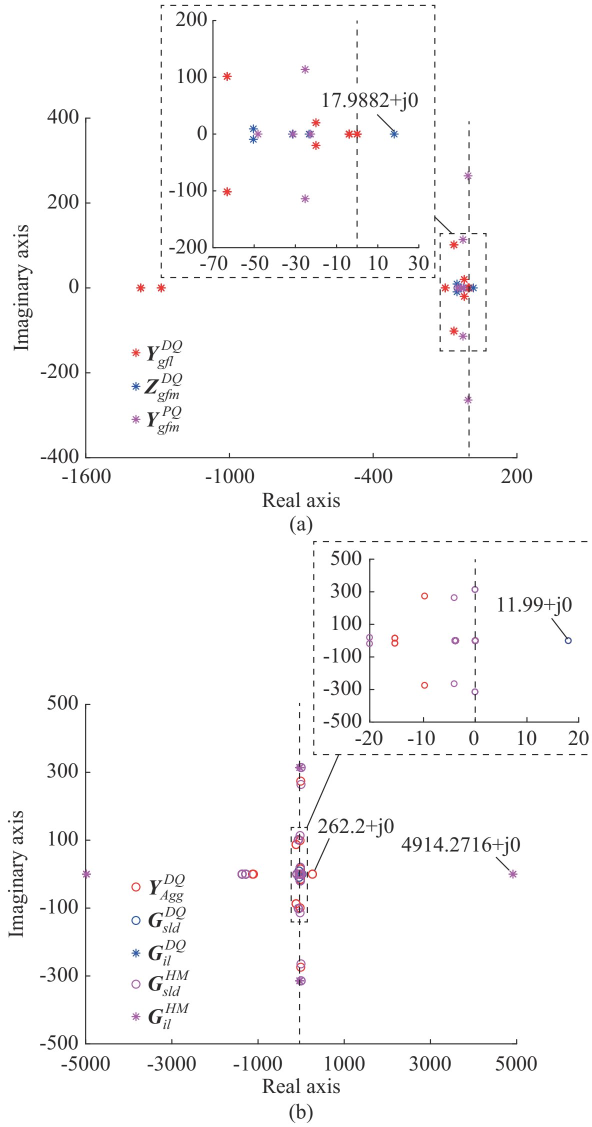


Fig. 8. Pole distribution of frequency-domain models of converters and two subsystems. (a) Frequency-domain models of converters. (b) Two subsystems.

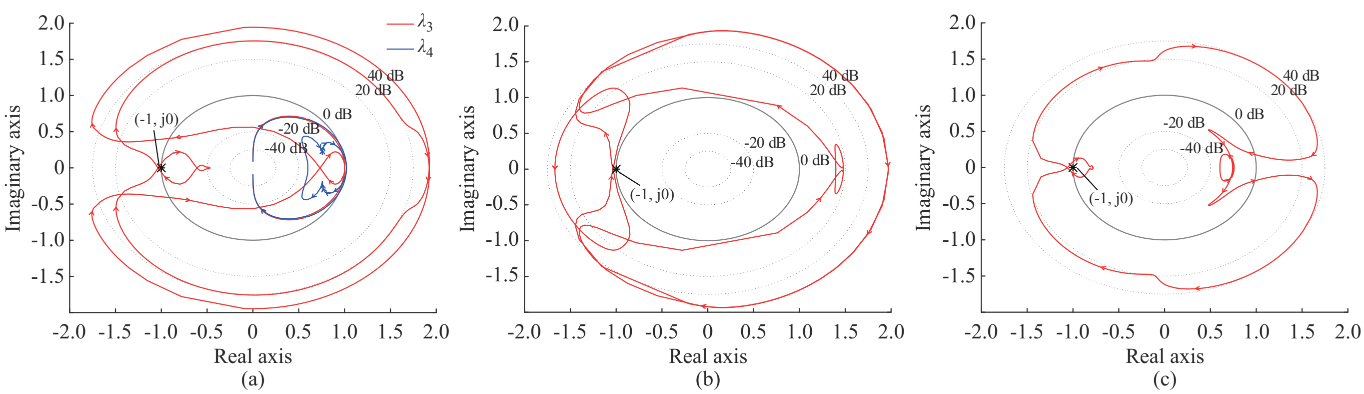


Fig. 9. Critical Nyquist curves of $\boldsymbol{L}_{sys}^{Agg}$, $\boldsymbol{L}_{sys}^{DQ}$, and $\boldsymbol{L}_{sys}^{HM}$. (a) $\boldsymbol{L}_{sys}^{Agg}$. (b) $\boldsymbol{L}_{sys}^{DQ}$. (c) $\boldsymbol{L}_{sys}^{HM}$.

The analysis conclusion aligns with the eigenvalue distribution, as well as the waveforms of the output current and active power at the point $B_1^{ac}$ depicted in Fig. 10(a) and (b), respectively. From Fig. 10(a), the unstable poles of the closed-loop system, obtained by solving $\boldsymbol{E}+\boldsymbol{L}_{sys}^{Agg}$, $\boldsymbol{E}+\boldsymbol{L}_{sys}^{DQ}$, and $\boldsymbol{E}+\boldsymbol{L}_{sys}^{HM}$ are consistent with the value of $3.019\pm\mathrm{j}95.36$. This observation demonstrates that the hybrid frequency-domain model yields the same conclusion as the *V-I* model, indicating that both models effectively evaluate the stability of power system. This conclusion is further supported by the FFT results from the output current at the point $B_1^{ac}$, which exhibits oscillation components at frequencies of 35 Hz and 65 Hz.

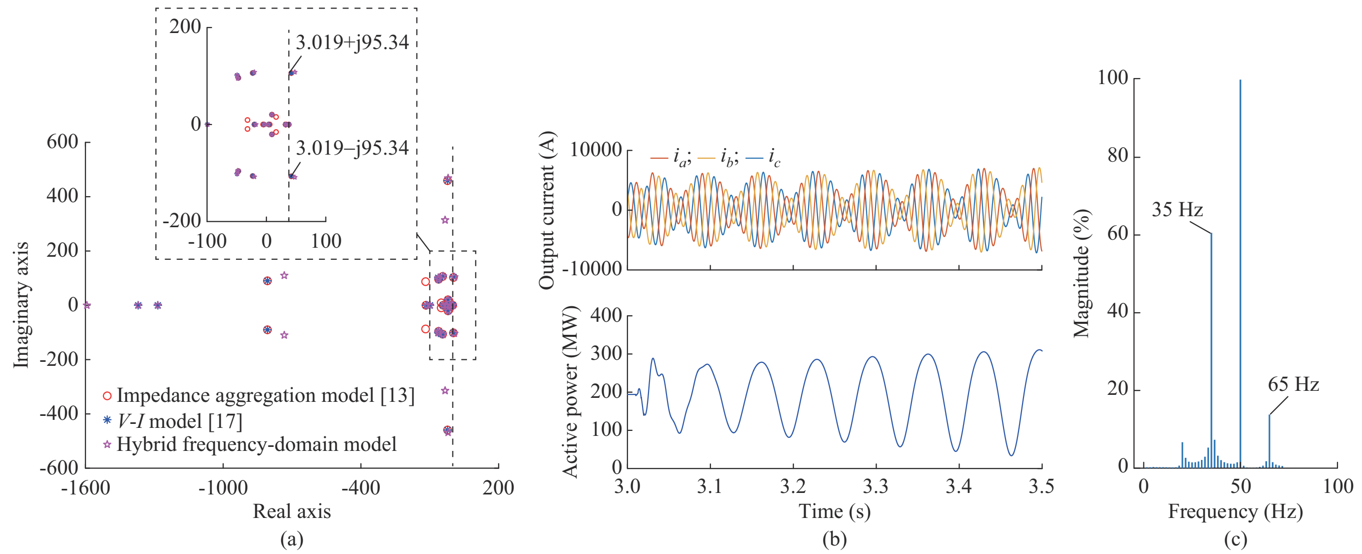


Fig. 10. Time-domain analysis results of multi-converter parallel system. (a) Eigenvalue distribution of closed-loop system. (b) Three-phase output current and active power waveforms at point $B_1^{ac}$. (c) FFT results from output current at point $B_1^{ac}$.

### *C. Discussion on System-level Stability Analysis Methods*

To assess the stability of power-electronics-based power systems, the frequency-domain analysis methods have emerged as a crucial analytical tool widely employed [17], [18], [29]-[31]. Based on the frequency-domain model of equipment, the system model is organized in various forms, including the nodal admittance matrix, the loop impedance matrix, the whole system closed-loop matrix, and the whole system open-loop gain matrix [30], [31]. By calculating the poles or zeros of these models, the system eigenvalues are obtained, subsequently determining the system stability and sensitivity. In contrast to the eigenvalue analysis methods based on the state space model, these methods do not necessitate a white box model of the system but only a gray box model or a back box model. However, these methods still entail a substantial computational burden when calculating eigenvalues, especially using measurement data [29].

Another commonly used stability analysis method involves employing the Nyquist criterion and the phase and gain margins from the Bode diagrams [17], [18], [29]. This method can give engineers intuitive results by graphical representation and impose less computational burdens, particularly in simulations or when utilizing measurement data [29], [32]. It should be emphasized that while our conclusions are derived from a mathematical model, they provide significant guidance for utilizing the GNC method based on a measurement model to assess system stability. In light of the finding that the *V-I* model of a self-stable GFM converter may exhibit potential RHP poles, employing impedance sweep data directly from the GFM converter to evaluate system stability could result in errors. The more suitable approach involves utilizing the measurement data of the $P/Q$-$\theta/V$ model, which can be converted from the impedance sweep data by (5).

Regrettably, unlike in single-input single-output (SISO) systems, obtaining system stability margin information through Bode diagrams is not feasible when analyzing multi-input multi-output (MIMO) systems using this method. Actually, the current research does not clearly define the stability margin of MIMO systems unless the MIMO system is decoupled into multiple SISO systems [33]. Neither the eigenvalue-based method nor the GNC-based method can determine the stability margin of the system. A potential solution could involve focusing the dominant Nyquist diagram in the application of GNC-based methods, akin to the focus of the traditional power system on the dominant eigenvalue. Further research is required to investigate the dominant Nyquist curve under varying working conditions and parameter designs.

## VI. Conclusion

This study highlights that there is no definitive guarantee that the poles of both the *V-I* model and the $P/Q$-$\theta/V$ model of a stable equipment reside exclusively in the left-half plane. To guarantee a frequency-domain model without an RHP pole, the applicability of frequency-domain models of self-stable converters is discussed. Following the design model, this study suggests that GFL converters are more suitably represented by an ideal current source in parallel with *V-I* admittance model, while GFM converters are more suitably represented by an ideal power source in parallel with $P/Q$-$\theta/V$ admittance model. According to the principle of equivalence, this paper proposes a hybrid frequency-domain modeling framework and stability criteria for grid-connected converter system with the frequency-domain models of GFL and GFM converters built in the *V-I* and $P/Q$-$\theta/V$ framework, respectively, which eliminates the requirements for checking RHP poles in the non-passive subsystem model when applying the Nyquist criterion. By avoiding this step, the complexity of modeling and stability analysis for complex systems is reduced.

## APPENDIX A

$$F_2 = K_g(K_g Q_{e0} + 1.5 L_g V_{ac0}^2 \omega_0) \tag{A1}$$

$$F_3 = K_g[K_g P_{e0} + (1.5sL_g + 1.5R_g)V_{ac0}^2] \tag{A2}$$

$$F_4 = K_g V_{ac0}[K_g P_{e0} + (-1.5sL_g - 1.5R_g)V_{ac0}^2] \tag{A3}$$

$$F_5 = K_g V_{ac0}(K_g Q_{e0} - 1.5 L_g V_{ac0}^2 \omega_0) \tag{A4}$$

$$z_{1,2} = -\frac{R_g}{L_g} \pm \mathrm{j}\omega_0 \tag{A5}$$

$$z_{3,4} = \frac{0.5(F_{12} \pm \sqrt{F_{13}})}{F_{11}} \tag{A6}$$

$$F_{11} = L_g^2 P_{e0}^2 + L_g^2 Q_{e0}^2 \tag{A7}$$

$$F_{12} = -2L_g P_{e0}^2 R_g - 2L_g Q_{e0}^2 R_g \tag{A8}$$

$$F_{13} = 9L_g^2 P_{e0}^2 V_{ac0}^4 + 9L_g^2 Q_{e0}^2 V_{ac0}^4 - 4L_g^4 P_{e0}^4 \omega_0^2 - 8L_g^4 P_{e0}^2 Q_{e0}^2 \omega_0^2 - 4L_g^4 Q_{e0}^4 \omega_0^2 \tag{A9}$$

where $z_{1,2}$ and $z_{3,4}$ are the zeros of $F_1$.

## REFERENCES


[1] J. Shair, H. Li, J. Hu *et al*., "Power system stability issues, classifications and research prospects in the context of high-penetration of renewables and power electronics," *Renewable and Sustainable Energy Reviews*, vol. 145, p. 111111, Jul. 2021.

[2] Y. Cheng, L. Fan, J. Rose *et al*., "Real-world subsynchronous oscillation events in power grids with high penetrations of inverter-based resources," *IEEE Transactions on Power Systems*, vol. 38, no. 1, pp. 316-330, Jan. 2023.

[3] B. Wen, D. Boroyevich, R. Burgos *et al*., "Analysis of *D-Q* small-signal impedance of grid-tied inverters," *IEEE Transactions on Power Electronics*, vol. 31, no. 1, pp. 675-687, Jan. 2016.

[4] R. H. Lasseter, Z. Chen, and D. Pattabiraman, "Grid-forming inverters: a critical asset for the power grid," *IEEE Journal of Emerging and Selected Topics in Power Electronics*, vol. 8, no. 2, pp. 925-935, Jun. 2020.

[5] F. Zhao, X. Wang, and T. Zhu, "Power dynamic decoupling control of grid-forming converter in stiff grid," *IEEE Transactions on Power Electronics*, vol. 37, no. 8, pp. 9073-9088, Aug. 2022.

[6] S. Fu, Y. Sun, J. Lin *et al*., "*P/Q-ω/V* admittance modeling and oscillation analysis for multi-VSG grid-connected system," *IEEE Transactions on Power Systems*, vol. 38, no. 6, pp. 5849-5859, Nov. 2023.

[7] S. Shah, W. Yan, V. Gevorgian *et al*., "Power-domain impedance theory for the analysis and mitigation of interarea oscillations," in *Proceedings of 2020 IEEE Power & Energy Society General Meeting*, Montreal, Canada, Aug. 2020, pp. 1-5.

[8] Z. Yang, C. Mei, S. Cheng *et al*., "Comparison of impedance model and amplitude-phase model for power-electronics-based power system," *IEEE Journal of Emerging and Selected Topics in Power Electronics*, vol. 8, no. 3, pp. 2546-2558, Sept. 2020.

[9] C. Li, J. Liang, L. Cipcigan *et al*., "DQ impedance stability analysis for the power-controlled grid-connected inverter," *IEEE Transactions on Energy Conversion*, vol. 35, no. 4, pp. 1762-1771, Dec. 2020.

[10] Y. Li, Y. Gu, Y. Zhu *et al*., "Impedance circuit model of grid-forming inverter: visualizing control algorithms as circuit elements," *IEEE Transactions on Power Electronics*, vol. 36, no. 3, pp. 3377-3395, Mar. 2021.

[11] X. Wang, F. Blaabjerg, and W. Wu, "Modeling and analysis of harmonic stability in an AC power-electronics-based power system," *IEEE Transactions on Power Electronics*, vol. 29, no. 12, pp. 6421-6432, Dec. 2014.

[12] W. Cao, Y. Ma, and F. Wang, "Sequence-impedance-based harmonic stability analysis and controller parameter design of three-phase inverter-based multibus AC power systems," *IEEE Transactions on Power Electronics*, vol. 32, no. 10, pp. 7674-7693, Oct. 2017.

[13] Z. Zou, J. Tang, X. Wang *et al*., "Modeling and control of a two-bus system with grid-forming and grid-following converters," *IEEE Journal of Emerging and Selected Topics in Power Electronics*, vol. 10, no. 6, pp. 7133-7149, Dec. 2022.

[14] G. Li, Y. Chen, A. Luo *et al*., "An enhancing grid stiffness control strategy of STATCOM/BESS for damping sub-synchronous resonance in wind farm connected to weak grid," *IEEE Transactions on Industrial Informatics*, vol. 16, no. 9, pp. 5835-5845, Sept. 2020.

[15] N. Liu, H. Wang, L. Sun *et al*., "Modular impedance modeling and stability analysis of hybrid AC/DC power systems with grid-forming and grid-following converters," *IEEE Access*, vol. 12, pp. 4063-4077, Jan. 2024.

[16] J. Samanes, A. Urtasun, E. L. Barrios *et al*., "Control design and stability analysis of power converters: the MIMO generalized Bode criterion," *IEEE Journal of Emerging and Selected Topics in Power Electronics*, vol. 8, no. 2, pp. 1880-1893, Jun. 2020.

[17] W. Cao, Y. Ma, L. Yang *et al*., "*D-Q* impedance based stability analysis and parameter design of three-phase inverter-based AC power systems," *IEEE Transactions on Industrial Electronics*, vol. 64, no. 7, pp. 6017-6028, Jul. 2017.

[18] Y. Li, Z. Shuai, X. Liu *et al*., "Stability analysis and location optimization method for multiconverter power systems based on nodal admittance matrix," *IEEE Journal of Emerging and Selected Topics in Power Electronics*, vol. 9, no. 1, pp. 529-538, Feb. 2021.

[19] J. Jia, X. Yan, B. Qin *et al*., "Modeling and analysis of the torque-frequency dynamics for multi-VSC parallel system based on the equivalent admittance," *IEEE Transactions on Power Delivery*, vol. 37, no. 5, pp. 3597-3607, Oct. 2022.

[20] Z. Yang, M. Zhan, D. Liu *et al*., "Small-signal synchronous stability of a new-generation power system with 100% renewable energy," *IEEE Transactions on Power Systems*, vol. 38, no. 5, pp. 4269-4280, Sept. 2023.

[21] Y. Xu, M. Zhang, L. Fan *et al*., "Small-signal stability analysis of type-4 wind in series-compensated networks," *IEEE Transactions on Energy Conversion*, vol. 35, no. 1, pp. 529-538, Mar. 2020.

[22] L. Harnefors, M. Hinkkanen, U. Riaz *et al*., "Robust analytic design of power-synchronization control," *IEEE Transactions on Industrial Electronics*, vol. 66, no. 8, pp. 5810-5819, Aug. 2019.

[23] F. Liu, J. Liu, H. Zhang *et al*., "Stability issues of *Z*+*Z* type cascade system in hybrid energy storage system (HESS)," *IEEE Transactions on Power Electronics*, vol. 29, no. 11, pp. 5846-5859, Nov. 2014.

[24] D. Yang and X. Wang, "Unified modular state-space modeling of grid-connected voltage-source converters," *IEEE Transactions on Power Electronics*, vol. 35, no. 9, pp. 9700-9715, Sept. 2020.

[25] L. Harnefors, M. Bongiorno, and S. Lundberg, "Input-admittance calculation and shaping for controlled voltage-source converters," *IEEE Transactions on Industrial Electronics*, vol. 54, no. 6, pp. 3323-3334, Dec. 2007.

[26] H. Wu, X. Ruan, D. Yang *et al*., "Small-signal modeling and parameters design for virtual synchronous generators," *IEEE Transactions on Industrial Electronics*, vol. 63, no. 7, pp. 4292-4303, Jul. 2016.

[27] K. M. Alawasa and Y. A. R I. Mohamed, "Impedance and damping characteristics of grid-connected VSCs with power synchronization control strategy," *IEEE Transactions on Power Systems*, vol. 30, no. 2, pp. 952-961, Mar. 2015.

[28] S. Liao, M. Huang, X. Zha *et al*., "Emulation of multi-inverter integrated weak grid via interaction-preserved aggregation," *IEEE Journal of Emerging and Selected Topics in Power Electronics*, vol. 9, no. 4, pp. 4153-4164, Aug. 2021.

[29] J. Sun, "Frequency-domain stability criteria for converter-based power systems," *IEEE Open Journal of Power Electronics*, vol. 3, pp. 222-254, Mar. 2022.

[30] J. Shair, X. Xie, W. Liu *et al*., "Modeling and stability analysis methods for investigating subsynchronous control interaction in large-scale wind power systems," *Renewable and Sustainable Energy Reviews*, vol. 135, p. 110420, Jan. 2021.

[31] Y. Zhu, Y. Gu, Y. Li *et al*., "Impedance-based root-cause analysis: comparative study of impedance models and calculation of eigenvalue sensitivity," *IEEE Transactions on Power Systems*, vol. 38, no. 2, pp. 1642-1654, Mar. 2023.

[32] W. Zhou, Y. Wang, R. E. Torres-Olguin *et al*., "Effect of reactive power characteristic of offshore wind power plant on low-frequency stability," *IEEE Transactions on Energy Conversion*, vol. 35, no. 2, pp. 837-

853, Jun. 2020.
[33] H. Zhang, X. Wang, M. Mehrabankhomartash *et al*., "Harmonic stability assessment of multiterminal DC (MTDC) systems based on the hybrid AC/DC admittance model and determinant-based GNC," *IEEE Transactions on Power Electronics*, vol. 37, no. 2, pp. 1653-1665, Feb. 2022.

**Ni Liu** received the B.S. degree in electrical engineering from East China Jiaotong University, Nanchang, China, in 2016, and the M.S. degree from University of Electronic Science and Technology of China, Chengdu, China, in 2019. Currently, He is working toward the Ph.D. degree in electrical engineering at Harbin Institute of Technology, Shenzhen, China. His current research interests include control of power electronic converters, power system stability analysis, and offshore wind power transmission system.

**Hong Wang** received the B.S., M.S., and Ph.D. degrees in electrical engineering from Harbin Institute of Technology, Harbin, China, in 1998, 2000, and 2004, respectively. He has been an Associate Professor with the School of Mechanical Engineering and Automation, Harbin Institute of Technology, Shenzhen, China, since 2010. His research interests include renewable energy system, electric motor drive design, electric vehicle control technique, and power electronics.

**Weihua Zhou** received the B.Eng. and M.Sc. degrees in electrical engineering from the Honors College, Northwestern Polytechnical University, Xi'an, China, in 2014, and the School of Automation, Northwestern Polytechnical University, in 2017, and the Ph.D. degree in power electronics from the Department of Energy Technology, Aalborg University, Aalborg, Denmark, in 2020. He is currently working in Australian Energy Market Operator, Melboume, Australia. His research interests include modeling, analysis, and control of inverter-based resource.

**Jie Song** received the B.E. degree in automation from Central South University, Changsha, China, in 2016, the M.S. degree in electrical engineering from Royal Institute of Technology, Stockholm, Sweden, in 2018, and the Ph.D. degree in electrical engineering from Technical University of Catalonia, Barcelona, Spain, in 2023. His research interests include novel tools for analysis and control of converter-based power networks.

**Yiting Zhang** received the B.S. degree in electrical engineering from Harbin Institute of Technology, Shenzhen, China, in 2022. She is currently working toward the M.S. degree in electrical engineering in Harbin Institute of Technology. Her research interests include distributed resource, high voltage direct current (HVDC), grid-forming control, and offshore wind power transmission system.

**Eduardo Prieto-Araujo** received the M.Sc. and Ph.D. degrees in industrial engineering from the School of Industrial Engineering of Barcelona, Technical University of Catalonia, Barcelona, Spain, in 2011 and 2016, respectively. He is currently a Serra Húnter Associate Professor in Technical University of Catalonia. His research interests include renewable generation system, control of power converters for HVDC applications, interaction analysis between converters, and power electronics dominated power system.

**Zhe Chen** received the B.Eng. and M.Sc. degrees in electrical engineering from the Northeast China Institute of Electric Power Engineering, Jilin, China, in 1982 and 1986, respectively, the M.Phil. degree in power electronic from Stafford-shire University, Stoke-on-Trent, U.K., in 1993, and the Ph.D. degree in power and control from the University of Durham, Durham, U.K., in 1997. He has been a Full Professor with the Department of Energy Technology, Aalborg University, Aalborg, Denmark, since 2002. His main research interests include wind power, power electronics, power system, and multi-energy system.